Defects and Reliability of GaN-Based LEDs: Review and Perspectives

Matteo Buffolo,* Alessandro Caria, Francesco Piva, Nicola Roccato, Claudia Casu, Carlo De Santi, Nicola Trivellin, Gaudenzio Meneghesso, Enrico Zanoni, and Matteo Meneghini*

Herein, the main factors and mechanisms that limit the reliability of gallium nitride (GaN)-based light-emitting diodes (LEDs) are reviewed. An overview of the defects characterization techniques most relevant for wide-bandgap diodes is provided first. Then, by introducing a catalogue of traps and deep levels in GaN and computer-aided simulations, it is shown which types of defects are more detrimental for the radiative efficiency of the devices. Gradual degradation mechanisms are analyzed in terms of their specific driving force: a separate analysis of recombination-enhanced processes, driven by nonradiative recombination and/or temperature-assisted processes, such as defects or impurity diffusion, is presented. The most common lifetime estimation methods and standards adopted for solid-state luminaires are also reported on. Finally, the paper concludes by examining which are the typical degradation and failure mechanisms exhibited by LEDs submitted to electrical overstress.

1. Introduction

The gallium nitride (GaN) material system represents the foundation of modern optoelectronics devices, such as light-emitting diodes (LEDs) and laser diodes (LDs). The wide bandgap range attainable by tuning the composition of the In- or Al-based alloys of GaN allows the fabrication of efficient optical emitters ranging from the green visible spectrum to the UV-C range. The market penetration of GaN-based optoelectronics was originally driven by the introduction of blue LEDs (450–480 nm), that ultimately allowed the creation of white luminaries based on efficient solid-state sources, rather than on conventional incandescent or halogen lamps. Nowadays, an increasing number of countries are progressively phasing out conventional light sources in favor of LED-based solutions, owing to their higher efficiency, higher brightness, longer lifetime, and lower environmental impact. LEDs are also continuously gaining market shares in the automotive lighting filed and are widely employed as backlighting solutions in TVs or displays. Regarding this latter market segment, researchers and industries are also pushing toward the development and adoption of displays based on blue and green micro-LEDs,[1–3] which are set to become the standard for high-contrast future displays for mobile and home entertainment. Moving toward the UV range, down to 260 nm, AlGaN-based solid-state emitters are becoming of utmost interest because they allow the fabrication of low-cost and efficient sanitation equipment for objects and surfaces,[4,5] for the purification of waste waters,[6,7] for bioagent detection,[8] and for curing applications.[9] Finally, visible LEDs are also becoming of interest for optical communications based on standard solid-state luminaires, which can allow direct free-space data transfer rates in excess of 1 Gb s^{-1}.[10,11]

A key parameter for optical sources is lifetime. For general lighting, a longer lifetime means that the luminaire needs to be replaced less often. This is highly beneficial for any application where any maintenance requires the temporary interruption of critical services, like tunnel street lighting, and in the automotive and aeronautic field. More than two decades of scientific and industrial research allowed state-of-the-art white LEDs to reach useful lifetimes in excess of 50 000 h, under nominal operating conditions. This was achieved by several improvements in doping strategy,[12] device structure,[12–14] package design,[15,16] and semiconductor crystalline quality.[17–19] However, if we consider the stability of the luminous output at low current densities, at longer emission wavelengths, or for less mature LED technologies such as GaN-based UV-C or micro-LEDs, several reliability-limiting factors are still under investigation. In several cases, a lifetime limiting factor is represented by

M. Buffolo, A. Caria, F. Piva, N. Roccato, C. Casu, C. De Santi, G. Meneghesso, E. Zanoni, M. Meneghini
Department of Information Engineering
University of Padova
35131 Padova, Italy
E-mail: matteo.buffolo@dei.unipd.it; matteo.meneghini@unipd.it

N. Trivellin
Department of Industrial Engineering
University of Padova
35131 Padova, Italy

N. Trivellin
Department of Information Engineering
University of Padova
35131 Padova, Italy

the generation/propagation of nonradiative recombination centers (NRRCs) or impurities in proximity of the active region of the devices occurring during operation. A higher defectiveness is typically exhibited by quantum well (QW) devices featuring higher indium content emitting at longer wavelengths,[20] and can severely impact luminescence in the low bias regime, where the radiative efficiency of the devices strongly depends on the balance between radiative and Shockley Read Hall (SRH) recombination. This effect is detrimental for backlighting or self-emissive solid-state displays, where a high image contrast and high visual dynamic range are to be preserved over the entire lifespan of the product.

Being based on a AlGaN, UV sources can also be affected by additional types of degradation processes,[21] more strictly related to dopant instability,[22] to the migration of hydrogen within the heterostructure,[23] or to reduction in injection efficiency, associated to defects generation and charge accumulation processes.[24]

Finally, for mature visible LED technologies, gradual degradation mechanisms act as secondary lifetime limiting processes compared to the electrical overstress events[25] that can induce the sudden and catastrophic failure of the devices.

The aim of the review article is to report on the main physical processes that limit the reliability of modern GaN-based LEDs. As device degradation is often caused by the migration or generation of some types of defects or impurities, this work begins with an overview of the main measuring techniques that allow the detection and characterization of traps and deep levels within GaN LEDs. These defects are then categorized and analyzed in terms of their capability of acting as nonradiative recombination centers, with the aid of technology computer-aided design (TCAD) simulations. A deeper overview is provided in relation to In-related defects because these are assumed to be the main reliability- and efficiency-limiting defects in long-wavelength GaN devices. The discussion will then move to the analysis of temperature- and recombination-enhanced degradation processes, focusing on Auger-driven and optically induced mechanisms. The article will then end with a short overview of the typical acceleration factors and lifetime estimation techniques that are nowadays employed by the solid-state lighting (SSL) industry to determine the operating life of devices and luminaires based on GaN solid-state sources. Finally, an analysis of the degradation processes that take place when GaN LEDs are operated in electrical overstress conditions will be presented.

2. Experimental Techniques for Defects Analysis

GaN has a periodic crystal structure that influences its properties as optical emitter. The presence of semiconductor defects can result in the interruption of periodicity, and modify the electro-optical performance of the devices. The consequence of this local perturbation is represented by the introduction of allowed energy states inside the forbidden bandgap of material. Native lattice defects (such as vacancies, antisite defects, or self-interstitials) can originate from a nonideal arrangement of host atoms during growth, which can be exacerbated in the presence of heteroepitaxial growth on foreign substrates.[26] On the other hand, the incorporation of foreign atoms (such as carbon, oxygen, magnesium, silicon) inside the crystal may induce the generation of other types of "impurity-related" (or extrinsic)

defects. The electronic states introduced by defects can either act as carrier traps or as nonradiative recombination centers. The presence of defects may limit both GaN LEDs' reliability and performance, reducing peak efficiency, contributing to the green gap,[27] and favoring efficiency droop.[27–29] It is therefore of primary importance to characterize the properties of the defects within the device, by identifying their energy position, trapping behavior, capture cross section and spatial location through appropriate measuring techniques. Additionally, the complete characterization of a trap or deep level allows to better infer on its physical origin.

Let us consider the simple case of an electron trapped in a deep level. The energetic transitions that this carrier can undergo with respect to the conduction band can be easily described in terms of its 1D configurational coordinate (CC) diagram,[30] as depicted in **Figure 1**. This kind of plot reports the total (electronic and vibrational) energy of the system in function of a generalized coordinate Q, which can be assumed to represent the average bond length between the atoms surrounding the defect (or equivalently the ensemble of their spatial coordinates). Here, the conduction band represents the excited state for the trapped electron, whereas the trap level is considered to be the ground state of the transition. The trapping of a charged carrier induces a variation in the local charge density that, in turn, affects the relative positions of the atomic nuclei nearby. The intensity of this variation strongly depends on the level of localization of the wave function of the trapped electron. In the case of an electron trapped in a shallow level, the wave function is delocalized (approximately in the order of several interatomic distances) and therefore it induces minimal changes to the local potential and to the position of the surrounding atoms, i.e., to Q. Conversely, deep levels exhibit a strongly localized wave function extending only in proximity of the defect, meaning that the
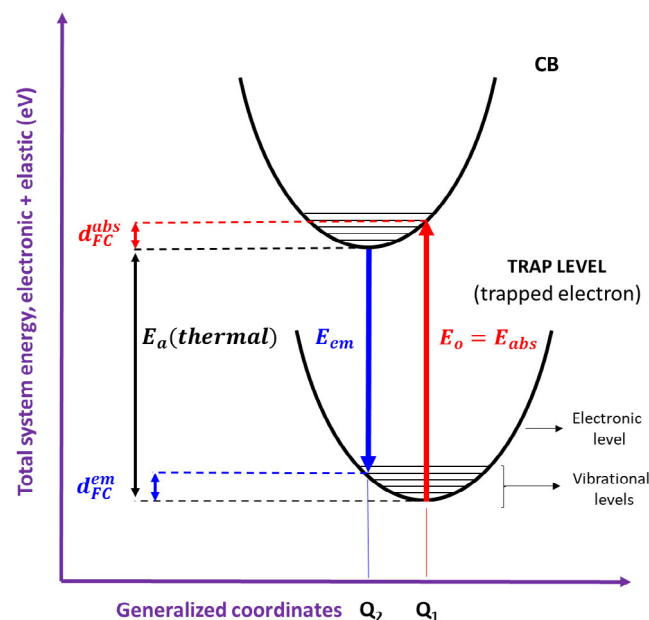
Figure 1. Generalized configurational coordinate diagram depicting the emission and capture processes between a trap level and the conduction band.

surrounding atoms are strongly influenced by the added electron-related charge. As a consequence, once a carrier is trapped these neighboring atoms have to rearrange their relative positions in order to accommodate the renewed charge distribution, thus reaching a new equilibrium position (named Q_1 in the CC diagram of Figure 1). The trapped carrier can then be promoted to the conduction band through two main processes: 1) the absorption of a photon (optical ionization), or 2) the thermal emission from the level (thermal ionization). In the first case, the electron is promoted to the excited state through a vertical transition: as optical transitions are fast compared to the average relaxation time of the host atoms (Franck–Condon approximation[31]), no variation in their relative position takes place. The characteristic photon energy determining the onset of optical ionization is labeled E_o in Figure 1. Once the deep level loses its carrier, neighboring atoms will rearrange their positions and reach a new equilibrium condition Q_2. As the minima of the ground and excited states differ in terms of configurational coordinates, i.e., $Q_1 \neq Q_2$, the promoted carrier will have to lose its excess energy in order to reach the energy minimum within the new lattice (and electronic + vibronic) configuration. The amount of energy that is lost through heat release during this process is called Franck–Condon shift, and is equivalent to the term d_{FC}^{abs} reported in Figure 1. The energy difference $E_o - d_{FC}^{abs}$ between the absorbed photon energy and the Franck–Condon shift is equivalent to E_a, which is the thermal ionization energy (or binding energy) of the trapped electron. This energy is equivalent to the difference in energy between the minima of the ground and excited states, and represents the amount of thermal energy that needs to be provided to the trapped carrier to induce its release through thermal ionization, and is usually referred to as the (thermal) activation energy of the trap.

Based on the considerations reported above, the CC diagram of a given trap level can be completely characterized once its E_o and d_{FC}^{abs} (or equivalently its E_a) are known. Additionally, in order to fully characterize the capture and emission properties of the level, one would also require to identify 1) the optical cross section (which expresses the photon absorption probability), 2) the other defect-related parameters it depends on,[32,33] 3) the apparent capture cross section, 4) its specific temperature dependency,[34] and 5) the concentration N_t of the deep level. Several advanced techniques can be used to characterize defects in semiconductor devices based on Schottky or p–n junctions, and featuring a space-charge region (SCR). These methods typically rely on the measurement of the variation in device capacitance induced by an external stimulus, like a voltage pulse, an optical pulse, a change in temperature, and so on. Information regarding the properties of the defects (i.e., density, activation energy, and cross section) are then derived from the electrical response of the device to the aforementioned stimuli. In the following paragraphs, we will briefly describe the techniques that are more relevant for p–n-like devices based on wide-bandgap materials. These include: capacitance deep-level transient spectroscopy (C-DLTS), relying on the measurement of the capacitance transient after a voltage pulse; thermal admittance spectroscopy (TAS), which evaluates the device admittance in function of frequency and temperature; deep levels optical spectroscopy (DLOS),

which relies on the measurement of the capacitance transient during an optical pulse of variable photon energy; and lighted capacitance–voltage (LCV) measurement, which evaluates the difference between the device capacitance in dark condition and the capacitance under an appropriate monochromatic light.

2.1. C-DLTS

The C-DLTS technique was developed by Lang et al.[35] and characterizes the emission processes of a trap by evaluating the transient in capacitance induced by a voltage pulse.

Figure 2 describes this process for a p^{++}–n junction (an equivalent explanation could be provided for n^{--}–p junctions, or for Schottky diodes), considering that a single donor level is present: one can see that there is an initial phase where the junction is biased at a certain voltage V_R for a certain amount of time, in order to reach the steady-state condition. When a filling pulse V_f is applied for a time t_{fp}, the width of the space charge region is decreased, and the Fermi level E_f is lifted, thus inducing the filling of the traps whose energy level E_T lies below E_f (i.e., capture of electrons). The decrease in SCR extensions causes an increase in capacitance, as indicated in Figure 2. At the end of the filling pulse, the voltage is returned to V_R and the capacitance transient is measured. After the bias returns to V_R, the deep level starts to emit previously trapped electrons toward the conduction band, and this results in a variation in capacitance according to

$$\frac{\Delta C(t)}{C(\infty)} = -\frac{n_T(t)}{2N_D} = -\frac{N_T}{2N_D}\exp(-e_n t) \tag{1}$$

where N_T is the total number of traps, $n_T(t)$ is the number of filled trap at time t, N_D is the doping of n-side, and e_n is the emission rate for the majority carriers. The measurement is then repeated several times by changing the sample temperature, thus enabling the analysis of the variation of the capacitance transient, and therefore of the characteristic emission constant, with temperature. Following the relation

$$\ln(\tau_n T^2) = (E_C - E_T) \cdot \frac{1}{kT} - \ln(\sigma_n \gamma) \tag{2}$$

the slope of the $\ln(\tau_n T^2)$ versus $\frac{1}{kT}$ plot represents the activation energy of the trap, whereas the intercept with the y-axis is proportional to the apparent capture cross section. Results of C-DLTS measurements are often reported by displaying the so-called rate-window plot. Derived from the technological limitations of the first capacitance samplers, this kind of plot shows the difference in capacitance evaluated after two intervals t_1 and t_2 from the end of filling pulse, in function of the measuring temperature. It can be demonstrated that as the trap emission rate varies with temperature, the plot shows a peak in correspondence of the temperature for which the emission rate is exactly the rate of the window, proportional to $(t_1 - t_2)^{-1}$. An example of a typical rate-window plot of a C-DLTS measurement is reported in **Figure 3**.

According to the theory, the shift of the peak position with temperature and rate window allows to extract the Arrhenius plot of the trap, whereas the magnitude of the peak provides information on trap density, as expressed by Equation (1). The main
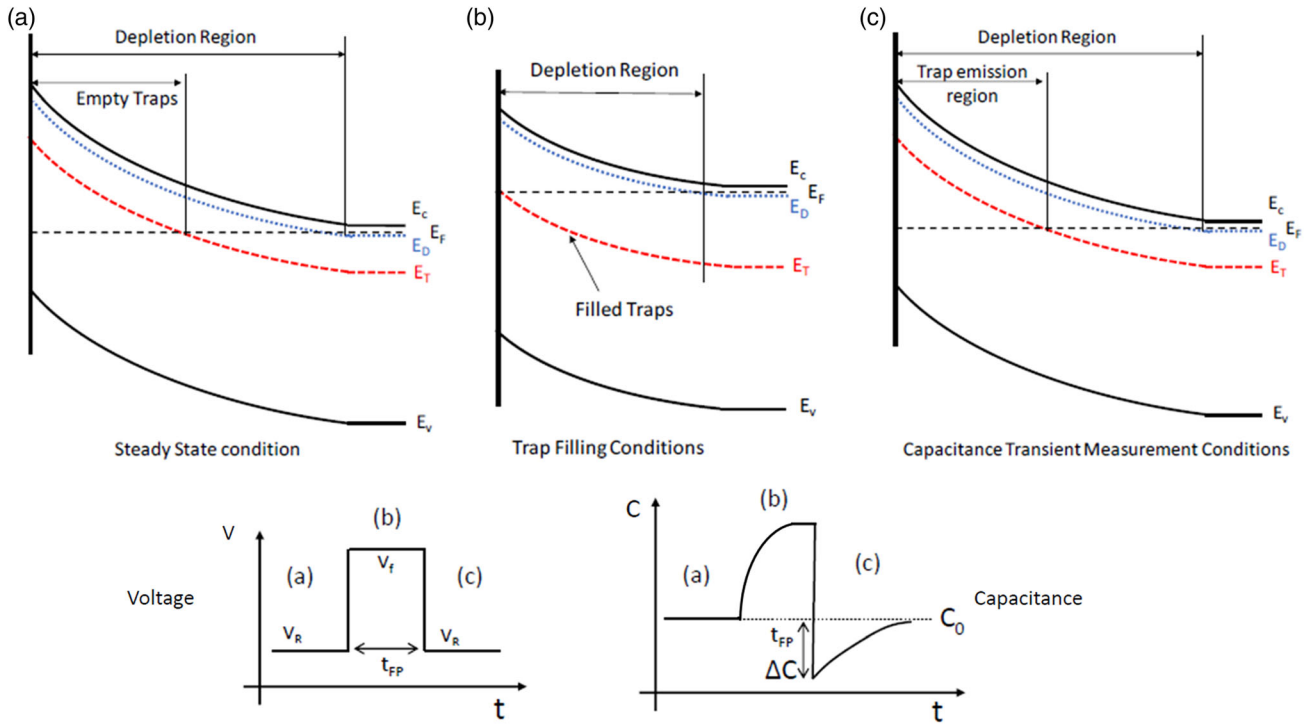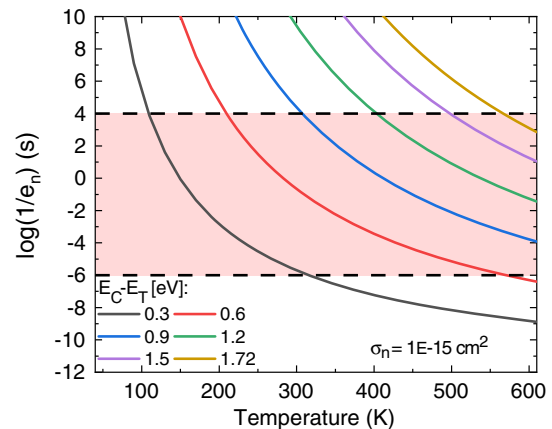
Figure 2. Variation of the band diagram during the capacitance transient measurement. a) Initial steady-state condition, b) trap-filling condition after the filling voltage pulse, and c) return to the steady-state condition, where the capacitance transient is recorded.
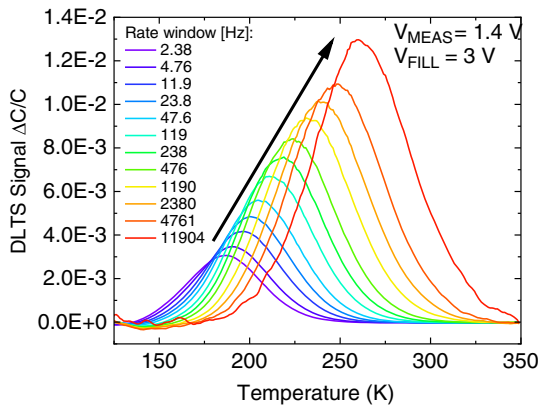
Figure 3. C-DLTS signal at different rate windows. Each rate window exhibits a peak at different temperatures, caused the changes in the trap emission rate with temperatures.

Figure 4. Variation of the characteristic emission time with temperature as a function of activation energies for an electron trapped in a deep level. An average capture cross section of 1E–15 cm^2 and the GaN-related N_c and electron effective mass values have been used for the calculation. The shaded region represents the time constants range that can be measured with conventional defects spectroscopy techniques (from the μs to the ks range). The 1.72 eV curve corresponds to a midgap level (at $T = 300$ K).

limitation of this measurement technique for wide-bandgap semiconductors is the impossibility to detect deep levels close to midgap, i.e., with higher E_a, if the sample is not heated up, and sufficient thermal energy is provided to the trapped carrier to allow its escape. If we consider the case of an electron trapped in a deep level, its thermal emission rate toward the conduction band at a given temperature can be expressed as

$$e_n = \frac{1}{\tau_n} = \frac{\sigma_n \nu_{th} N_c}{g} \exp\left(-\frac{E_C - E_T}{kT}\right) \tag{3}$$

where N_c is the effective density of conduction band states reported to the band edge, $\nu_{th,n}$ is the electron thermal velocity, and g is the degeneracy of the level. The variation of the time constant of the emission process with temperature expressed by Equation (3) is reported in **Figure 4**, for different trap energies.

ADVANCED SCIENCE NEWS
www.advancedsciencenews.com

pssa
physica status solidi a
www.pss-a.com

Figure 4 shows that by means of conventional spectroscopy techniques, which are able to detect time constants in the μs to 10^4 s range, deep levels close to the midgap of GaN can only be characterized if either the measurement period is extended beyond 1–10 ks, which may not be practically feasible, or if the device temperature is raised above 500–600 K. As temperatures above some hundreds of degrees Celsius may be required, and those temperatures could damage the device,[36–38] other techniques, such as DLOS, have been developed to overcome this issue.

2.2. TAS

TAS is a technique that evaluates the variation of the capacitance C and the conductance G of a junction, in function of frequency and temperature.[39,40] By increasing the frequency during a capacitance measurement, it is possible to evaluate the emission rate of a trapped carrier. This is achieved by considering that the trap responds by capturing and emitting carriers during the two semiperiods of the applied AC signal until a certain frequency ω_{rf}, above which the emission and the capture processes become too slow compared to the AC measurement frequency. It is possible to demonstrate that at that frequency the $\frac{G(\omega)}{\omega}$ shows a peak in its spectrum, and that this frequency is proportional to the emission rate of the trap. Therefore, by repeating the measurement at different temperature it is possible to reconstruct the signature of the trap, as described for the C-DLTS technique. TAS is often applied to GaN Schottky diodes and GaN-based LEDs, but due to technical temperature and frequency limitations, only shallow defects are typically detected. As a matter of fact, measuring frequencies in the range of 0.1–5 MHz and measuring temperatures ranging from 75 to 470 K have been reported to only allow the identification of relatively shallow levels in GaN-based diodes, with activation energies from tens of meV to 0.35 eV.[40–44] This is also the case of the Mg used in these type of structures as p-dopant (see, for instance, refs. [42-45]). TAS shows a lower sensitivity with respect to C-DLTS and suffers from a stronger influence from the parasitic resistive components.[46] On the other hand, TAS can be used for narrow-gap materials and/or shallow defects, for which the emission rate is too fast to be measured with the standard transient methods.

2.3. DLOS

With respect to the previous techniques, DLOS allows to extract the optical characteristics of a deep level, including its optical ionization energy, the spectral dependence of the optical cross section $\sigma_O(h\nu)$, also called photoionization cross section (PCS), and the steady-state photocapacitance (SSPC).[47]

The theory of DLOS has some similarities with DLTS because both techniques evaluate the capacitance transient due to the carrier emission from the traps; DLTS employs a voltage pulse to fill the trap before the emission phase, whereas DLOS relies on an optical pulse to induce the emission of trapped carriers.[33] Slow optical transients can also be investigated by SSPC measurements, during which the device is biased at the reverse voltage V_R, chosen depending on the extension of the space charge region that has to be characterized. At a certain time, a pulse of monochromatic light is applied to the device in order to excite all the deep levels through the absorption of a photon, resulting in an emission of previously trapped carriers. In case of emission of majority carriers, the capacitance will increase; vice versa, it will decrease if minority carriers are emitted. Once the new steady-state condition is reached and the capacitance stabilizes, the light stimulus is removed; the carriers are then allowed to be captured again by the traps and the device is brought back to the initial condition. A schematic representation of the SSPC measurements is reported in **Figure 5**.

A relatively simple analysis based on the capacitance transients can be performed to evaluate trap density N_T from SSPC, and to estimate the trap level E_T, the optical ionization energy E_O, and the Frank–Condon energy d_{FC} from the PCS spectrum (E_O is the minimum energy required for a photon to promote an electron or hole from a localized bandgap state, whereas d_{FC} is approximately the amount energy released in the form of multiphonon emission to the lattice atoms close to the defective sites where photon absorption occurs, as depicted in Figure 1). The aforementioned information can be gathered by repeating the transient measurement under monochromatic light of different wavelengths, thus obtaining the SSPC and the PCS spectra reported in **Figure 6**.

The value of N_T can be extracted from the SSPC spectrum, considering that the variation of $\frac{\Delta C}{C}$ in function of the incident photon energy $h\nu$ is expressed by the formula

$$\frac{\Delta C}{C} \cong \frac{N_T}{2N_D} \cdot \frac{\sigma_n}{\sigma_n + \sigma_p} \qquad (4)$$

where N_D is the donor concentration, assuming to be dealing with a p^{++}–n junction and donor traps, evaluated from a
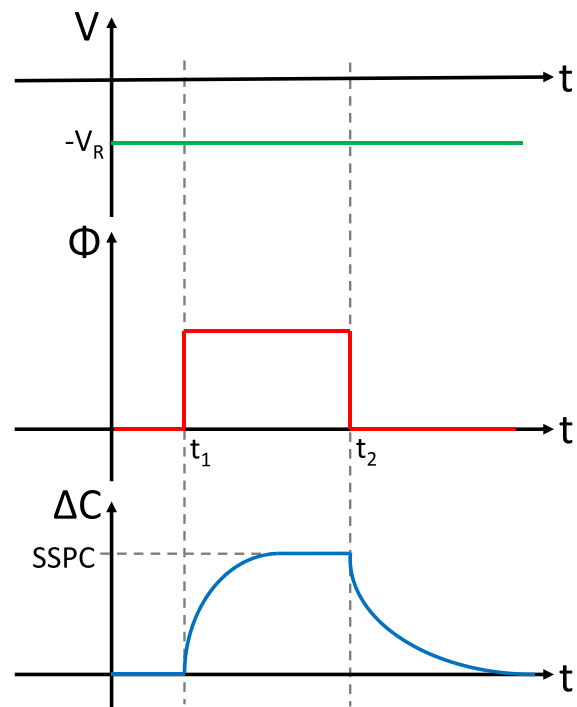
Figure 5. Trends of measuring voltage, photon flux Φ, and capacitance variation ΔC during a SSPC measurement.
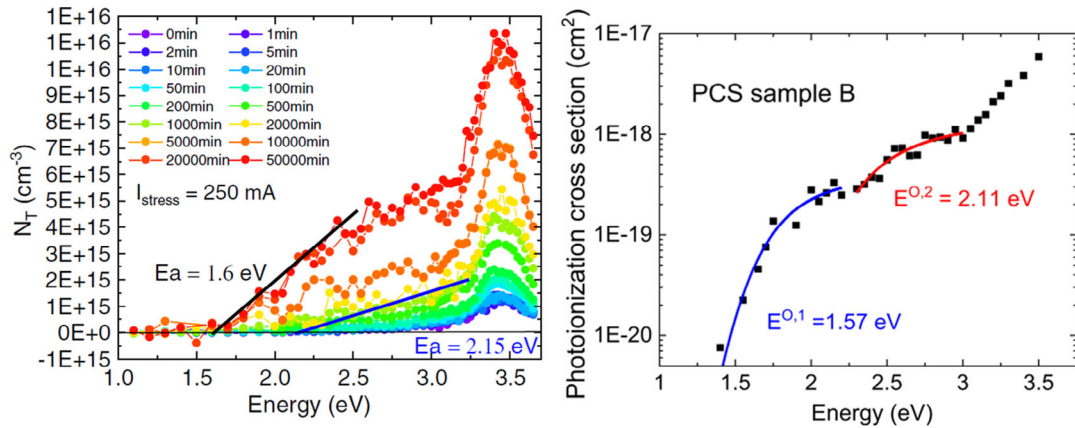
Figure 6. (Left) SSPC measurement during a constant current stress on UV-C LEDs. It shows an increase in the traps concentration during the stress test, in particular the increase in concentration of a midgap defect at 2.15 eV. Reproduced with permission.[24] Copyright 2021, The Optical Society. (Right) PCS measurement and relative fit to extract the optical activation energies of the traps in InGaN single quantum well (SQW) LEDs. Reproduced with permission.[74] Copyright 2021, IOP Publishing.

C–V measurement, and $\sigma_{n,p}$ are the capture cross sections. This formula can be further approximated in the condition $\Delta C \ll C$, resulting in: $\frac{\Delta C}{C} \cong \frac{N_T}{2N_D}$. Considering the SSPC spectrum, every change in its slope identifies an individual deep level because slope variations correspond to the onset of emission of carriers from different deep levels; these changes occur at the energy $h\nu = E_O - d_{FC}$, due to the previously described phonon-assisted photoionization process. In order to calculate the energy depth of the defect, both E_O and d_{FC} need to be known. The measurement is completed by the extraction of the PCS: this is done by evaluating the initial derivative of the capacitance transient $\left(\frac{d\Delta C}{dt}\right)_{t=0} \propto \left(\frac{dn_t}{dt}\right)_0$, just after the beginning of the illumination.[33] Trap analysis is then performed through the formula proposed by Pässler,[32] given by

$$\sigma(h\nu, T) \simeq \frac{\text{constant}}{h\nu\sqrt{2\pi d_{FC}\varepsilon\coth(\frac{\varepsilon}{2k_BT})}} \times \int_0^{+\infty} dE_k \frac{E_k^{3/2}}{(E_k + E^O - d_{FC})^2}$$
$$\times \exp\left[-\frac{(h\nu - E^O - E_k)^2}{2d_{FC}\varepsilon\coth(\frac{\varepsilon}{2k_BT})}\right] \tag{5}$$

where ε is the effective phonon energy and E_k is the kinetic energy of the excited electron, equal to the difference between the increase in electronic energy between the two states and the thermal ionization energy E_a associated to the trap state. Equation (5) shows that, under some specific model-related assumption,[32] ε, E_O, and d_{FC} completely determine the photon energy- and temperature-related dependencies of σ^o. Thus, from the analysis of the experimental data, the related optical ionization energy and Franck–Condon shift can be evaluated. Once the presence of a deep-level is established, the profile of its concentration within a certain device region can be carried out by repeating the transient measurement at a fixed monochromatic light and variable voltages, in order to change the extension of the portion of SCR under investigation. By choosing the right monochromatic light, which in specific cases allows the detrapping only a specific defect, it is possible to follow its concentration in the region explored through the voltage sweep. This type of measurement exhibits some drawbacks and limitations, part of which can be overcome by leveraging the LCV method described in the following paragraph.

2.4. LCV Measurements

LCV method is used to provide a profile of the traps in a junction also when the condition $N_T \ll N_D$ is not satisfied. The LCV technique is based on the evaluation of the difference in voltage and capacitance between two capacitance–voltage measurements where the traps are filled (dark condition) and empty (light condition). To this aim, two different methods can be employed: the recording of the change in junction voltage at fixed capacitance and the recording of the change in junction capacitance at fixed voltage. The first implementation of this technique was proposed by Brotherton,[48] and required the knowledge of the difference in voltage ΔV needed to maintain the same junction capacitance C when a deep level is filled compared to when it is empty. Thus, by differentiating ΔV with respect to C, it is possible to calculate a profile of the deep level $N_T(x)$

$$\Delta V = \frac{q}{\varepsilon}\int_0^{x_D} x n_T(x) dx \tag{6}$$

where $n_T(x)$ is the trap concentration in function of the position, x_D is the limit of the SCR, and x is the position within the SCR. If $n_T(x)$ is assumed constant and equal to N_T in a region between x_1 and x_2, it is possible to extract the deep-level concentration in that region, as done by Armstrong,[26] through the relation

$$N_T = \frac{\varepsilon}{q}\frac{\Delta V}{\int_{x_1}^{x_2} x dx} \tag{7}$$

An example of the implementation of this technique was provided by Piva et al.,[49] where the authors studied the efficacy of the insertion of a superlattice underlayer (SL UL), aimed at blocking the growth of defects toward the active region in an
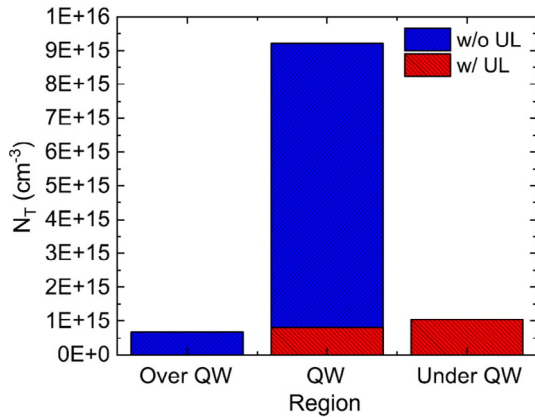
Figure 7. Trap concentrations calculated by means of the LCV method. The explored region includes the active region and the layers closer to electron blocking layer (EBL) for the sample without UL. For the sample with UL, both the active region and the region toward UL were explored. Reproduced with permission.[49] Copyright 2020, IOP Publishing.

InGaN-based LED. As shown in **Figure 7**, the authors evaluated traps concentration N_T with the formula reported above and found a higher quantity of defects within the active region of the sample without the UL. This result confirmed both the efficacy of the UL and the defect blocking effect of the first In layer in the structure (this topic will be later addressed in Section 3.2).

A further improvement in the technique was presented in the study by Brotherton.[48] Let us consider the n-side of a junction, where the trap levels are sufficiently deep to be always occupied unless optically emptied, and assume that only one level per time can be optically emptied (by incident light of appropriate wavelength). Under these assumptions, the only change within the space charge of the depletion region in a steady-state illuminated condition would be due to a change in the deep levels occupancy. In these conditions, the calculation of $N_T(x)$ can simply be computed as the difference in net fixed charge densities determined via LCV scans taken under dark and monochromatic light conditions.

LCV is a method that provides a lower bound estimate of N_T because 1) not all deep levels contribute to the measured capacitance variation, 2) the calculation does not consider the distance λ between the end of SCR and the crossing between the trap level and the E_F (the so-called Debye tail), and 3) because for photon energies higher than $E_G/2$ electrons can be promoted from the valence band into the deep level, which prevents the complete emptying of the levels under steady-state condition.

3. Defects in GaN LEDs

3.1. Properties of GaN-Related Defects

The properties of the electrically and/or optically active lattice defects identified by means of the characterization techniques presented in the previous section can be employed to identify the defect species within the space-charge region of the semiconductor devices. This goal can either be achieved through simulations or through the comparison with other reports. Following this latter approach, we summarize in **Table 1** and

Table 1. Activation energies range for most common traps found in GaN- and AlGaN-based devices. The energy trap level is calculated from midgap; therefore, the plus sign indicates that trap is close to the conduction band whereas the minus sign indicates that trap is near to the valence band. Table mostly based on the data from Bisi et al.[51]

Type of defect or impurity	$E_T - E_{fi}$ [eV]
Native defects	
Nitrogen interstitial	From +0.66 to +0.96
Nitrogen vacancy	From +1.45 to +1.63
Nitrogen antisite	From +1.05 to +1.2
Gallium vacancy	+0.60, +1.08, +1.12, +1.48, and from −0.86 to −0.89
Gallium interstitial	From +0.81 to +0.92
Extended defects	From +0.60 to +1.55
Impurities-related	
Hydrogen	+1.23, +1.58
Iron	From +1 to 1.32
Carbon	From +1.23 to 1.58 and from −0.77 to −1.43
Magnesium	+1.12, +1.36, −1.64
Oxygen	From +0.60 to+ 1.21
Silicon	From +1.32 to 1.35

Figure 8 traps information collected from more than 100 scientific publications.

Energy levels within the gap can act as efficient recombination centers, if they are close to midgap. The recombination rate through the deep level of energy E_t and concentration N_t can be calculated through the Shockley Read Hall theory.[50] Under the assumption of small deviations of carrier densities from equilibrium within an intrinsic material, and considering equal holes and electrons capture rates, the simplified SRH recombination-related lifetime can be expressed as

$$\tau_{SRH} = \tau_{n0}\left[1 + \cosh\left(\frac{E_t - E_{fi}}{k_B T}\right)\right] \quad (8)$$

where E_t is the depth of the trap level and τ_{n0} is equal to

$$\frac{1}{\tau_{n0}} = N_t v_{tn} \sigma_n \quad (9)$$

where v_{tn} and v_{tp} are the electrons and holes thermal velocities, whereas σ_n and σ_p are the respective apparent carrier capture cross section of the trap. Equation (8) shows that the lifetime has its minimum when the argument of the cosh function is zero, meaning that the trap level is at or close to midgap. This situation represents the worst case because $\tau_{SRH} = 2 \cdot \tau_{n0}$, and traps act as effective nonradiative recombination centers. Therefore, considering the dependencies exhibited by Equation (8), and the data from our catalogue on GaN defects,[51] we built the graph reported in **Figure 9**.

The goal of this analysis is to evaluate which are the experimentally-determined trap levels that are most detrimental for the internal quantum efficiency of the devices, at equal temperature and defect density condition. To this aim we reported a scatter plot of the values of activation energies versus respective apparent cross section contained in our catalog, on top
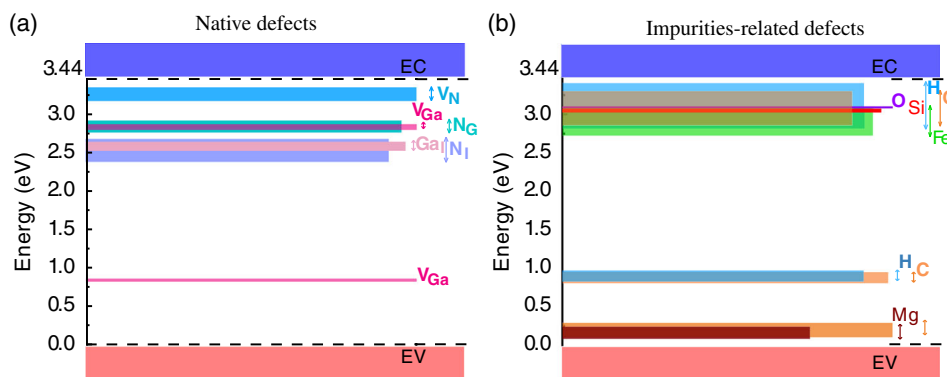
Figure 8. Position of the most common a) native and b) impurities-related defects within the bandgap of GaN. Extended defects have been omitted for clarity.
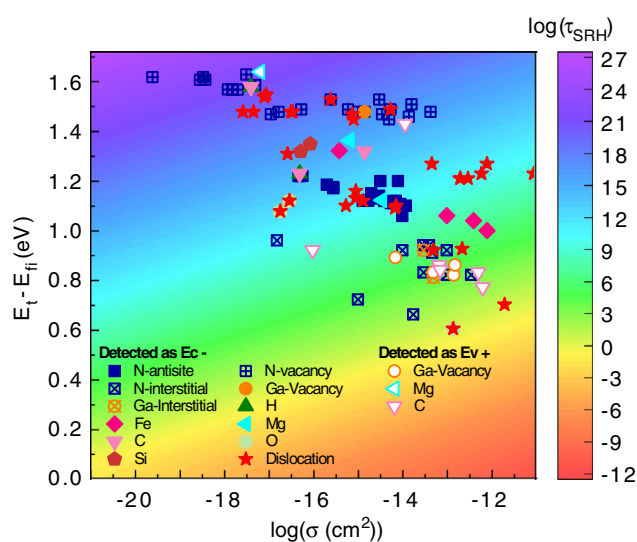
Figure 9. Plot of trap level in function of capture cross section, expressed in log scale, of experimentally characterized deep levels commonly found in GaN (only trap levels with associated physical origin have been included). The underlying heatmap represents the logarithm of the SRH lifetime at 300 K normalized for trap concentration $N_t = 10^{15}$ cm^{-3}.

of a heat/cool-coded map that represents the magnitude of the SRH lifetime at 300 K (i.e., hotter areas means a faster SRH recombination). Figure 9 shows that defects with a specific attributed origin tend to accumulate in a certain plot region, indicating that their physical nature and properties make them less or more detrimental for the radiative efficiency of the material. Regarding the latter group, we can see that trap signatures ascribed to nitrogen interstitials, extended defects, and C-related defects appear to offer the worse combination of activation energies and apparent cross sections.

N-vacancies (V_N) may originate potential NRRCs[19] when they form complexes with indium atoms[52,53] or with gallium vacancies, resulting in this latter case in V_N–V_{Ga} divacancies.[54] However, their low activation energy, 90 meV $< E_a <$ 270 meV, and small capture cross section, 2.5×10^{-20} cm^2 $< \sigma < 4.4 \times 10^{-14}$ cm^2, does not allow to mark isolated V_N as the most worrying species in

terms of nonradiative SRH recombination. While the probability of V_N formation in p-type GaN is higher than that of Ga-vacancy (V_{Ga}),[55] this latter species was identified as the dominant acceptor level in hydride vapor-phase epitaxy (HVPE) GaN-based LEDs.[56] Despite their energy level is close to the valence band, mostly reported within the 0.59 eV $< E_T - E_v <$ 1 eV range, the presence of V_{Ga} can lead to a reduction in the optical efficiency of LEDs because 1) it may prevent hole transport inside the active region,[17] 2) induce the formation of complexes, such as V_{Ga}–3H, V_{Ga}–2H, V_{Ga}–O_N–2H, V_{Ga}–O_N–H, V_N–V_N, which act as NRRCs[57,58] and/or release hydrogen during device operation.[59]

The identified impurities collected in our catalog are: Mg, H, Si, C, Fe, and O. From our analysis, oxygen-related defects appear to be the most critical in terms of SRH recombination because they are close to midgap and feature relatively big apparent capture cross sections. Look et al.[56] identified O_N as the dominant donors in HVPE GaN-based LED grown on Al$_2$O$_3$. Iron-related defects are often found in GaN high electron mobility transistor (HEMT) because Fe can be introduced as compensating species during bulk growth[60] to reduce the n-type conductivity of unintentionally intrinsically doped (u.i.d.) GaN layers, but they are not typically observed in LEDs. Si is used as n-dopant for the GaN buffer layer, and the few traps whose physical origin is believed to be related to silicon are shallow (90 meV $< E_a <$ 120 meV), with small capture cross section (10^{-18} cm^2 $< \sigma < 10^{-17}$ cm^2). Also, interstitial carbon can introduce deep levels close to midgap, with 1.2 eV $< E_C - E_T <$ 1.35 eV[61–64]; therefore an excessive carbon incorporation in the active region can contribute to the reduction in radiative efficiency of the devices.[17] Finally, the presence of magnesium and hydrogen in GaN-based devices is strictly correlated because part of the Mg introduced during growth may bond with residual H coming from the reactor chamber. It is found that their complexes can form efficient NRRCs.[65,66]

3.1.1. Impact of Spatial Trap Location

The presence of defects within or close to the active region can favor SRH recombination and drastically lower the radiative efficiency of the devices.[67] To better evaluate this aspect, we implemented TCAD simulation deck aimed at studying the
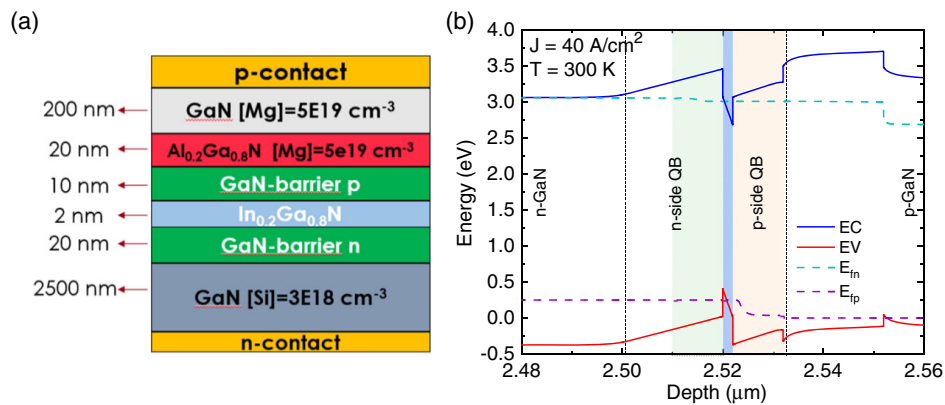
Figure 10. a) Implemented structure in the simulation deck. The simulated structure is a SQW InGaN\GaN LED. b) Band diagram of the reference structure with no traps, simulated at 40 A cm^{-2}. The regions inside the shaded rectangles are, respectively, a half of the n-side GaN barrier, the QW, and the p-side GaN barrier. We simulated the effect of traps located inside these regions on the LED optical performance.

impact that traps location, rather than trap type, has on the optical performance of a typical blue InGaN SQW LED. The simulated structure, shown in **Figure 10**a and implemented by means of Crosslight Apsys software suite, consists of a 2.5 μm n-GaN:Si layer ($N_D = 3 \times 10^{18}$ cm^{-3}), a 20 nm quantum barrier (QB) (labeled n-side QB), a 2 nm In$_{0.2}$Ga$_{0.8}$N QW, a 10 nm QB (labeled p-side QB), a 20 nm Al$_{0.2}$Ga$_{0.8}$N p-doped EBL ($N_A = 5 \times 10^{19}$ cm^{-3}) and a 200 nm p-doped GaN:Mg layer ($N_A = 5 \times 10^{19}$ cm^{-3}).

The band diagram of the ideal structure with no traps, simulated at an injection level of $J = 40$ A cm^{-2}, is shown in Figure 10b. We highlighted with different colors the regions where traps have been selectively introduced. In particular, we evaluated the effect of traps located inside a 10 nm slice of the GaN barrier on the n-side (green region), inside the QW (blue region), and in the 10 nm GaN barrier on the p-side (orange region): to allow a fair comparison, traps in the quantum barriers occupy the same volume. The adopted trap parameters are the following: donor type, $N_T = 5 \times 10^{16}$ cm^{-3}, capture cross section $\sigma = \sigma_n = \sigma_p = 1 \times 10^{-15}$ cm^2, and $E_C - E_T = E_g/2$. The very high

trap concentration and the midgap placing of the trap level constitute a worst case scenario as far as SRH recombination is concerned: the nonradiative lifetime is in the order of some ns, which is quite low for a state-of-the-art LED; nevertheless, these values were chosen to better highlight the impact of trap location on the optical performance of the device.

As shown in **Figure 11**, the optical emission of the device is strongly affected by the presence of NRRCs within the active region. In both bias conditions, we can see that 1) the optical power (OP) decay is the highest when traps are placed within the QW, where electron and holes densities reach their maximum and the SRH recombination rate (proportional to carrier density) is then maximum, 2) a milder effect is achieved when traps are placed within the GaN-barrier on the n-side, 3) a limited reduction in emission occurs if traps are located closer to the p-side. The higher reduction in optical efficiency for QW traps, and at lower bias level, is in agreement with the expected trend suggested by SRH theory. On the other hand, we see a strong unbalance in the effect of QB traps, which appear to be more detrimental if located at the n-side. This trend can be explained
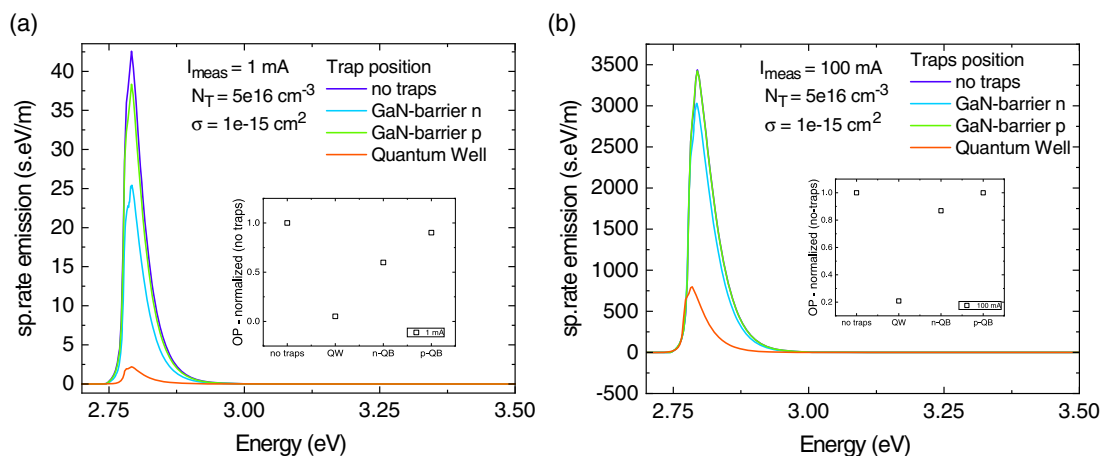
Figure 11. a) Simulated spontaneous emission spectrum at $I = 1$ mA, and b) at 100 mA, as a function of traps position inside the structure. The inset graphs show the relative OP normalized to the reference scenario in which no traps were included in the structure.

by considering that within the explored bias range traps can effectively reduce the density of electrons injected from the n-side due to recombination in the barriers, and this can lower the density of carriers reaching the QW region.

3.2. Role of Indium

The QWs of visible GaN-based LEDs are composed of ternary InGaN alloys. By tuning the indium content, these semiconductor materials theoretically allow to manufacture LEDs emitting over a wide range of wavelengths, from the UV-A to the infrared spectrum.[68] The purity of the InGaN crystal and the optimization of the growth technique are crucial to attain high levels of efficiencies and long useful device lifetimes.[69,70] For this reason, investigating how indium interacts with the epitaxial substrate and influences the lattice quality is extremely important. The presence of indium within the QWs has a strong impact on the radiative efficiency of the device. First, an increase in the indium concentration, which is associated to the reduction of the $In_xGa_{1-x}N$ growth temperature at high x values,[17] leads to an increase of the defectiveness of the active region,[20] and therefore to an increase in SRH-related recombination processes. In addition to that, radiative efficiency is also lowered as a consequence of e/h reduced wave function overlap induced by the quantum-confined stark effect (QCSE)[71] that results from the presence of the internal polarization fields. This reduction in radiative efficiency at increasing In mole fraction, and therefore decreasing bandgap and emitted photon energy, is referred to as "green gap".[27] Its dependency on material quality is caused by the interplay of multiple factors: first of all, a higher indium concentration reduces the lattice matching with the surrounding GaN barriers, thus increasing lattice strain. This leads to a full or partial relaxation of the InGaN layer that significantly degrades the properties of the QW.[72] Besides, it was recently shown that In-containing layers can favor the segregation of defects located on the GaN surface.[18,19] It has been proposed that these surface defects have an intrinsic origin, most likely related to nitrogen or gallium vacancies, and that they form in GaN grown at high temperature. In particular, considering that the low GaN stability at high temperature induces nitrogen atoms to dissociate from the surface and to form N_2 molecules, thus leading to the generation of nitrogen vacancies (V_N) at the surface, this specific kind of native defect is reasonably believed to interact with indium atoms and to form nonradiative recombination centers. This is not the only valid theory because the physical origin of such defects is still under investigation. A second hypothesis considers the presence of divacancies ($V_N - V_{III}$), as discussed in previous studies,[19,54,73] which may be associated to deep defects located near midgap. Acting as efficient NRRCs, these defects negatively affect the radiative efficiency of the device. By analyzing InGaN LEDs through DLOS and LCV, Armstrong et al.[26,28] identified two optically active defects at $E_C - 1.62\,eV$ and $E_C - 2.76\,eV$ in $In_{0.13}Ga_{0.87}N$ layers, as well as a level at $E_C - 2.11\,eV$ in GaN layers. It was found that the defect concentration 1) is significantly higher in the In-rich layers with respect to GaN layers, and 2) is proportional to the threading dislocation (TD) density, which was not found to influence the type of deep levels detected in the QWs, but only their concentration. These results

suggested that the identified defects derive from the interaction between dislocations, or other point defects, and the TDs generating NRRCs. Similar results have been reported also in previous studies[17,74,75] where the same midgap level has been measured. It is worth noticing that the presence of In-related defects does not influence negatively the emission only through the increase in SRH recombination, whose effects are more evident not only at low current injection levels,[76] but also through other processes that are more relevant in high current regime, like the defect-assisted Auger recombination process that will be described in Section 4.2. As the defect-assisted Auger coefficient is supposed to depend on trap concentration,[77] within high indium content QWs this recombination process can dominate over other recombination processes, being favored by both an high carrier concentration and crystal defectiveness.

As briefly stated in the previous paragraph, another effect of the increased lattice mismatch at increasing In content is a greater accumulation of piezoelectric charge at the interfaces between the well and the barriers. The induced piezoelectric field increases band bending, thus reducing the overlap between the electrons and holes wave functions. This ultimately reduces the probability of radiative transitions within the QW, resulting in a reduced internal quantum efficiency for longer wavelength LEDs due to the QCSE.[78] Additionally, due to the lower bimolecular recombination probability, injected carriers would tend to recombine not radiatively, thus favoring recombination-enhanced degradation processes (see the related discussion in Section 4.2).

Finally, an important observation concerns the difficulty of growing InGaN layers with a homogeneous indium concentration[79]: this could lead to fluctuations in the indium molar content within the QW, thus altering the ideal charge distribution and the peak emission wavelength.[80]

3.2.1. Mitigation Strategies

By exploiting the aforementioned capability of In-rich layers of incorporating defects, different techniques have been implemented in order to improve the efficiency of InGaN/GaN LEDs. A first approach leverages the introduction of an InGaN UL prior to the growth of the active region. The In content within the UL is lower with respect to the QW to avoid the photon reabsorption.[75,81,82] The insertion of an InGaN UL provides 1) a significant increase in the optical efficiency (see **Figure 12**) and 2) a great reduction in trap concentration within the active region. It was also found that 3) the detectable deep levels remain the same, regardless of the presence of the UL, demonstrating that the UL only modifies the concentration but not the type of defects within the active region (i.e., no new defects are generated by the presence of the UL). In addition, it was also shown that 4) defects suppression is proportional to indium molar content. In fact, it was not possible to achieve the same results by replacing InGaN with GaN grown at lower temperature, and thus with low defects concentration, which indicates that the presence of indium atoms has a determining impact on defect generation.[19,49,75]

The use of a UL can be beneficial for blue LEDs; on the other hand, the situation is different for near-UV LEDs, where
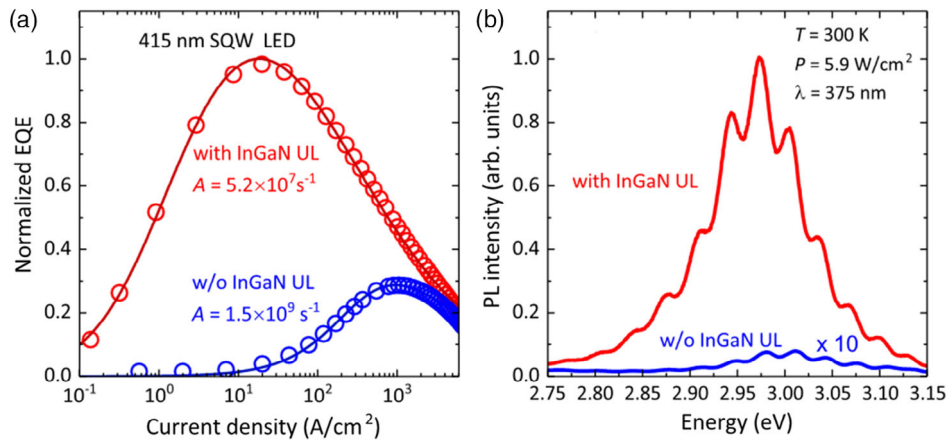
Figure 12. The comparison between a) the EQE and b) the PL intensity at 300 K of a SQW $In_{0.12}Ga_{0.88}N$ LED grown on GaN/sapphire template with and without a 55 nm $In_{0.03}Ga_{0.97}N$ UL. Reproduced with permission.[18] Copyright 2017, AIP Publishing.

significant light absorption taking place in the InGaN UL could affect the external efficiency of the devices. Reducing the indium content in the UL is not a good solution because the incorporation of "surface defects" directly depends on the total amount of In atoms. This would require an increase in the thickness of the InGaN UL, and this may favor the degradation of the surface morphology. A good alternative is the use of AlInN UL, because with a bandgap of ≈4.6 eV it would ensure transparency in the NUV range, as well as the possibility to implement thinner layers, owing to the greater In content (a molar fraction of 17% is required to obtain a good lattice matching with GaN layers).[83–85] The adoption of AlInN UL can strongly improve the efficiency of NUV LEDs, but still presents some drawbacks. First of all, the AlInN material quality rapidly degrades as the layer thickness is increased. To mitigate this issue, a particular structure composed of an AlInN/GaN SL UL with very thin layers (e.g., 2.1/1.75 nm) has been proposed.[49,74,83] This structure grants a greater improvement in the efficiency, but a critical issue still remains because a considerable spontaneous polarization mismatch at the AlInN/GaN interfaces is generated. This leads to a negative fixed charge density which creates a barrier for electrons. The detrimental effect of this electrostatic barrier can be mitigated by introducing a highly n-doped layer on top of the SL UL. This produces a positive fixed charge that compensates the piezoelectric charge, thus favoring the electron injection toward the active region.

The efficacy of this approach is demonstrated by **Figure 13**, which shows that the insertion of AlInN/GaN SL UL effectively reduces defect concentration in the active region of an InGaN violet LED.

4. Degradation Processes of GaN LEDs

This section deals with the analysis of the main gradual and sudden degradation processes impacting on the long-term reliability of GaN LEDs. As the driving forces of such processes are multiple (including photon density, temperature, carrier and current densities, etc.), each set of mechanisms will be separately treated.
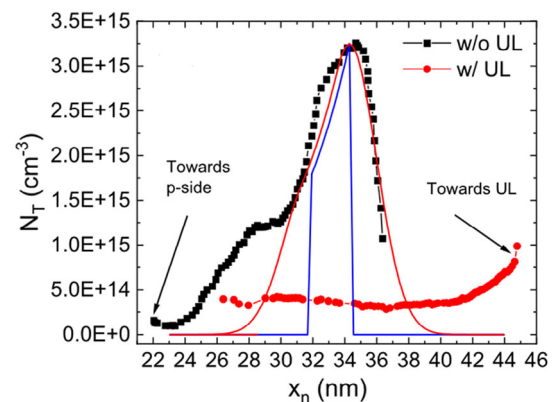
Figure 13. The comparison between the defect density profile of a SQW $In_{0.10}Ga_{0.90}N$ LED with and without a GaN /$In_{0.17}Al_{0.83}N$ SL UL (1.75/ 2.1 nm). The blue line represents the model of the NRRCs incorporation in the QW, while the red line is the convolution of the model with a Gaussian profile featuring a width of 5 nm. It can be noticed that the presence of the UL induces a significant reduction in the defect density inside the active region. Reproduced with permission.[49] Copyright 2020, IOP Publishing.

4.1. Thermally Activated Processes

This first section deals with the temperature-activated degradation processes that may impact the optical and electrical characteristics of the LEDs. In modern LEDs, especially in high-power devices, there is a high-intensity current flowing through the device that generates a non-negligible amount of heat, mainly due to Joule effect, contributing to the increase in junction temperature.[86]

Table 2 reports the specifications of four different commercial high-power blue LEDs. The junction-to-solder pad thermal resistances advertised by the manufacturer range from 1.3 to $10\,K\,W^{-1}$, depending on the size and on the type of the package employed. Considering these values, an increase in junction temperature up to 17.5 K with respect to the ambient temperature can be estimated, when the device is biased at its absolute maximum current. The estimation is quite optimistic because

ADVANCED
SCIENCE NEWS
www.advancedsciencenews.com

physica
status
solidi
a
www.pss-a.com

Table 2. Typical values of the junction-to-solder pad thermal resistance ($R_{th,jsp}$), absolute maximum current (I_{max}), voltage (V_{max}), and approximate OP (OP_{max}) at I_{max} for four different commercially available high-power blue LEDs. The two ΔT columns report the estimated difference in junction temperature with respect to ambient temperature when the device is biased at I_{max} and when thermal resistance R_{th} values equal to $R_{th,jsp}$ and to $15\,K\,W^{-1}$ are considered, respectively.

Manufacturer	Series	I_{max} [A]	V_{max} [V]	OP_{max} [W]	$R_{th,jsp}$ [K W^{-1}]	ΔT [K]	ΔT, $R_{th} = 15$ [K W^{-1}]
OSRAM	OSLON Square	2	3.15	3.75	1.3	3.3	38.3
Lumileds	Luxeon C	1	3.25	1.1	2.8	6	32.3
Lumileds	Rebel	1	3	1.35	10	16.5	24.8
Cree	XLamp XP-E	1	3.5	1.25	9	17.5	33.8

1) at high operating junction temperatures the dissipated power may be higher, due to the lower optical efficiency, and 2) because the junction-to-ambient thermal resistance can be much higher with respect to $R_{th,jsp}$, as evidenced by the results reported in the study by Buffolo et al.[87] in relation to similar high-power LEDs. Based on these results, we can assume that, in the best scenario, the junction-to-ambient thermal resistance should be higher than $15\,K\,W^{-1}$, which leads to ΔT values in excess of $38\,K$. The amount of self-heating strongly depends on the adopted cooling solution and on the temperature that the heat sink reaches during prolonged operation: as this component can reach values as high as $80\,°C$,[88,89] even though typical target design values are around $60\,°C$,[90] modern high-power LEDs may operate at junction temperature well in excess of $120\,°C$, which may lead to reliability- and performance-related issues.

LEDs are particularly sensitive to the operating temperature, since at higher junction temperatures a number of processes can contribute to the decrease in optical efficiency and to device degradation, which shorten the lifetime of the solid-state source. When a device is operated at high temperatures and in high-injection regime, i.e., when the current flow is high and QWs are filled with carriers, there can be a considerable escape of carriers from QWs both toward quantum barriers and toward the EBL (**Figure 14**a).

The rate of escape is a function of 1) current density and 2) temperature because those parameters determine the amount of carriers that can overcome the potential barriers, as well as 3) of indium (or aluminum, for the EBL) content because its relative concentration determines the effective barrier height. For reference, the height of the escape barrier between the QW and the QBs at increasing QW indium content is shown in Figure 14b: we can clearly see that for short-wavelength InGaN emitters, i.e., for near UV-A LEDs, the barriers heights can be relatively low (e.g., lower than 160 meV for electrons and lower than 40 meV for holes in the case of 405 nm emitters). The aforementioned temperature and structure-dependent loss process may lead to a decrease in efficiency with consequences on device temperature and reliability.[91]

Nonradiative SRH recombination rate is temperature-dependent, and this results in an increase in SRH losses at high temperatures.[50] The rate of SRH recombination may also change when the devices are subject to degradation: the energy released by SRH recombination events may promote the generation of further defects in the device[57,92,93] or locally increase lattice temperature, in a positive-feedback loop.

Buffolo et al. observed a remarkable dependence on stress temperature of the degradation of the reverse leakage current reported in **Figure 15**.[91] The reverse leakage is related to defect density; therefore, there is a temperature-related defect creation mechanism.

Also, diffusion processes that will be analyzed more in depth in Section 4.3 are enhanced by the temperature because diffusion coefficient D is temperature-dependent through Arrhenius law

$$D = D_0 \exp\left(-\frac{E_a}{k_B T}\right) \tag{10}$$

where D_0 is an exponential prefactor, E_a is the activation energy for the diffusion process, k_B is the Boltzmann constant, and T is
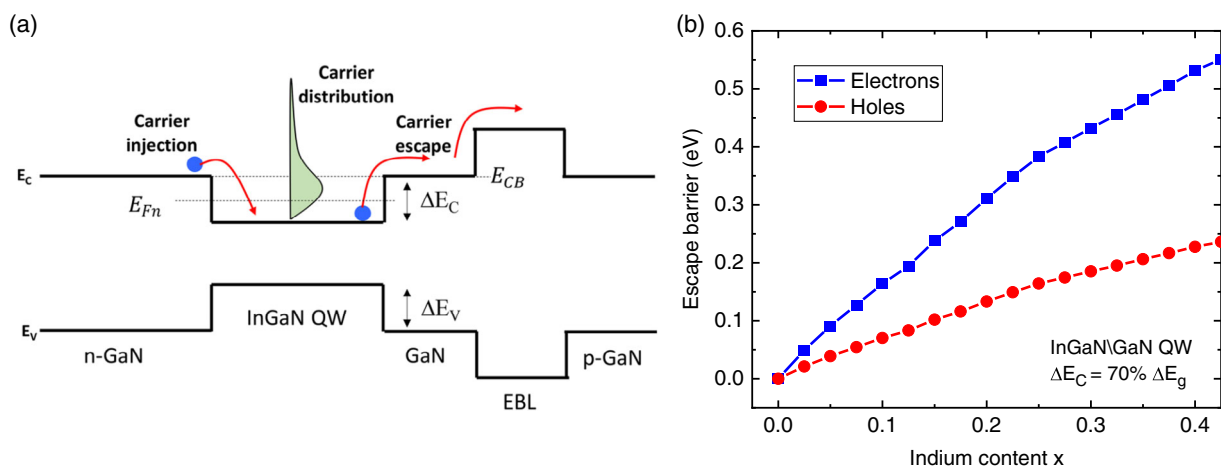
Figure 14. a) Schematic representation of the carrier escape mechanisms occurring with the active region of a InGaN–GaN LED in high injection regime. Reproduced with permission.[149] Copyright 2020, AIP Publishing. b) Escape barrier for electron (blue curve) and holes (red curve) with respect to indium content x in In$_x$Ga$_{1-x}$N-GaN QWs, calculated considering a 70:30 ratio between conduction and valence ratio discontinuity.[150,151]
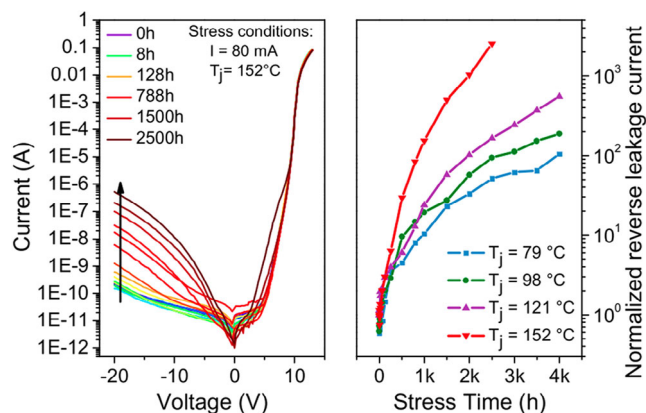
Figure 15. I–V curves of midpower white LEDs stressed at $T_j = 152\,°C$ (left) and normalized reverse leakage current of devices stressed at different T_j. Reproduced with permission.[91] Copyright 2015, Elsevier.

the temperature. By increasing the operating temperature also diffusion coefficient increases: if defects have a relatively low migration barrier (below 1 eV), the diffusion coefficient is significantly increased by temperature. This process can be enhanced by the presence of native defects.[94] Meneghini et al. performed a series of iso-current stress at 1 A and different ambient temperatures, from 60 to 120 °C, corresponding to junction temperatures ranging from 108 to 192 °C.

They found a decrease of the time to failure (TTF$_{90\%}$, i.e., the time needed to have a decrease of 10% in optical power) with an Arrhenius-like dependence on temperature, as shown in **Figure 16**. Samples stressed at low temperature showed a degradation process with an activation energy of 0.27 eV that was attributed to the increase in nonradiative recombination rate in the active region of the LED. This process was found to be driven by the carrier flow at moderate temperatures.

Another effect of the temperature is the degradation of the Ohmic contacts of the device, especially when the device is
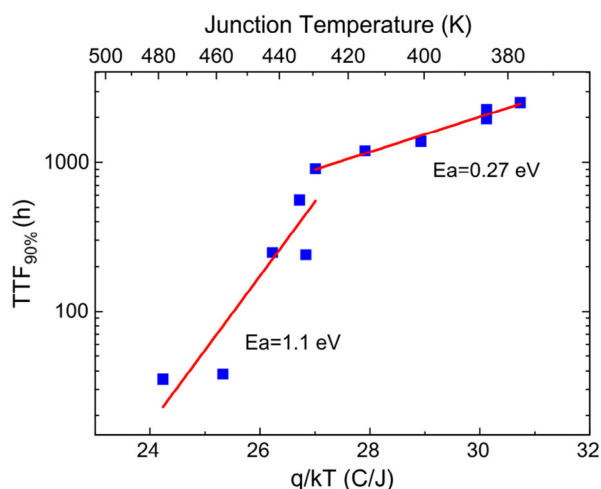
Figure 16. Arrhenius plot for TTF$_{90\%}$ during iso-current stress at 1 A and various junction temperatures. Reproduced with permission.[152] Copyright 2012, Elsevier.

submitted to high temperatures. This is the case of the second process shown in Figure 16, which is activated at junction temperatures above 140 °C. During high-temperature stress, the LEDs showed a decrease in optical power and an increase in the turn-on voltage. The process was found to have an activation energy approximately equal to 1.1 eV, and was ascribed to the degradation of the Ohmic contact at the p-side,[95] possibly related to Mg–H interaction that leads to the reduction in hole density and increases series resistance. In a step-stress experiment where current was gradually increased, Buffolo et al. observed that, by rising baseplate temperature, device failure and series resistance degradation occurred at lower stress current levels, possibly due to the stronger self-heating of the device, favored by the higher ambient temperature.[87]

Moving from chip to package level, there are several mechanisms that can affect LED reliability because high temperature is detrimental for the color-converting phosphors, the encapsulant material, and the housing. Commercial white LEDs showed a considerable chromaticity shift during aging, which was found to be strongly dependent on stress temperature.[96] Meneghini et al. performed a long-term thermal stress of phosphors by increasing stress temperature from 85 to 145 °C that led to a browning of the phosphor and lowering in color temperature of the converted light.[97] Also metallizations can suffer from thermal stress, due to the thermal mismatch between the materials used for their fabrication.[76] Moreover, thermal cycles that occur during repeated turn on/turn off can cause device failure due to the mechanical stress that causes delaminations and cracks at the interface between silicone and polycarbonate lens.[98]

4.2. Recombination-Enhanced Degradation

4.2.1. Auger-Driven Degradation

Degradation in GaN-based devices can also be assisted by other types of recombination events, such as Auger recombination. Ruschel et al.[99] studied a series of UV-B LEDs during a series of constant current stresses of 1000 h and identified an optical degradation process possibly related to Auger recombination. The authors found a correlation between the optical power decay and the inverse of the cube of the stress current density and developed a mathematical model for OP decay based on the equation

$$\text{OP}(t \gg \tau) = -\beta \cdot \ln(\alpha \cdot j^3 \cdot t) \tag{11}$$

where α and β are two fitting parameters, and τ is a characteristic time associated to the onset of the optical degradation mechanism. In order to extend the model to the whole operation time, the authors modified the previous equation by considering the initial condition $\text{OP}(t = 0) = 1$, thus obtaining the following relation

$$\text{OP}(t) = -\beta \cdot \ln\left(\alpha \cdot j^3 \cdot t + e^{-\frac{1}{\beta}}\right) \tag{12}$$

This model was reused by Piva et al.[24] to fit the optical power degradation at low current levels, exhibited by AlGaN UV-C LEDs during stress (**Figure 17**). Also, in this case the model fit perfectly
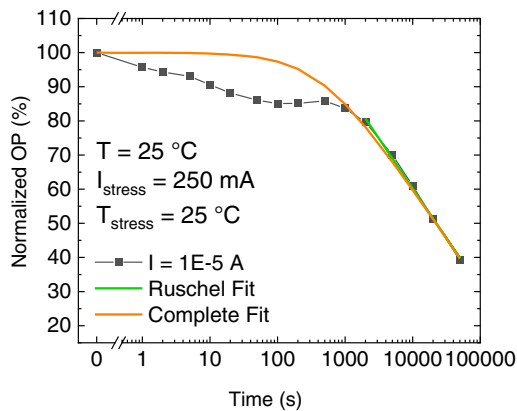
Figure 17. Fit of the optical power behavior at low current levels (10 µA) with the model proposed in the study by Ruschel et al.[99] The devices under test were commercial UV-B LEDs with nominal current of 350 mA, stressed at 250 mA at room temperature for 300 h. Reproduced with permission.[24] Copyright 2020, The Optical Society.

Figure 18. a) Correlation between the A and D coefficients; b,c) band diagrams for possible high-order process involving a trap: b) electron Auger scattering into a trap followed by SRH recombination with a hole from the trap, c) *eeh* Auger process where the trap level acts as a virtual state. Reproduced with permission.[27] Copyright 2019, American Physical Society.

the experimental data, allowing the authors to conclude about a possible correlation between the optical power degradation and the Auger recombination events occurring within the active layer of the devices.

Recent reports[27,77,100] suggested a new type of Auger-driven recombination process, different from the classical Auger recombination, which depends on the presence of defects. To accommodate the existence of this new mechanism, the authors replaced the classical ABC model with the following one
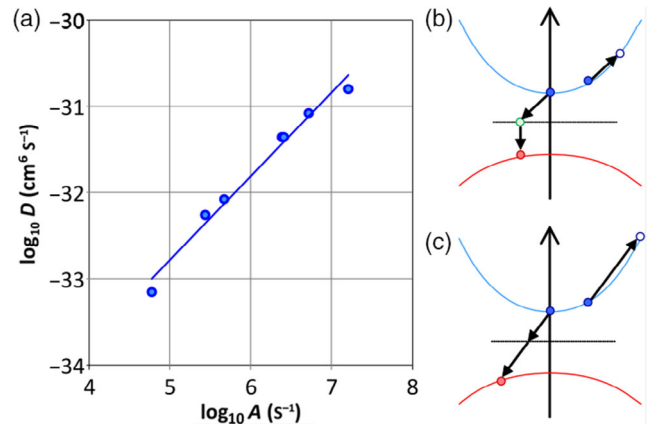
$$-\frac{dn}{dt} = An + Bn^2 + Cn^3 + Dn^2 \tag{13}$$

where D is called the defect-assisted Auger recombination coefficient. This coefficient is proportional to the A coefficient, and is used to take into account the Auger recombination events that promote an electron from the conduction band to higher energy levels, while the other electron recombines with a hole through a trap level. As in the canonical ABC model, A represents the non-radiative recombination coefficient, B is the radiative recombination coefficient, and C is the Auger recombination coefficient.[101] The correlation between the factors D and A and the sketch of the described processes are reported in **Figure 18**, which ultimately shows that the defect-assisted Auger coefficient is supposed to be intrinsically linked and proportional to SRH recombination, as it depends on the trap concentration.[77]

This mechanism could play an important role in the degradation of GaN optoelectronic devices, due to its quadratic dependence on carrier density and due to its relation with trap concentration. Additionally, it could partially explain the efficiency droop of green GaN LEDs at high injection levels.[27] As this recombination mechanism has just recently been proposed, its impact on LED lifetime has not been fully evaluated, yet.

4.2.2. Optically Induced Degradation

Photon-induced degradation is a type of degradation that mainly affects laser diodes, which are affected by phenomena like mirror coating damage or catastrophic optical damage (COD),[102] but acquired importance with the progresses in high-power LEDs. While the optical power density inside the laser cavity is very high, as it is required to attain the lasing condition, nowadays also high-power LEDs feature very high power density levels, up to several hundreds of W/cm² in projection LEDs.[103] Photons can induce various phenomena in the semiconductor material, depending on their energy and intensity. Typically, for impulsive damage, the pulse duration has a key role on degradation mechanisms: low energy pulses delivered on a short period of time determine the damage to the device. For example, very short pulses in the sub-nanosecond range (150 ps pulses at 36 TW cm^{-2} intensity, with an energy density of 5.4 nJ cm^{-2}) directly damage the material,[104] whereas longer pulses in the nanosecond range, with energy densities around 10 J cm^{-2}, mainly have thermal effects due to defect-driven absorption that may also be related to clusters of indium atoms.[105–107] These damages were observed when submitting LEDs to high-power laser pulses. In commercial LEDs, there are also some forms of optically induced degradations at package level, like encapsulant degradation and, in white LEDs, phosphors degradation. These photodegradation mechanisms, activated in combination with high temperatures, lead to the lowering in emission efficiency and to chromaticity shift due to the change in relative emission ration between blue (chip) emission and yellow (phosphor) emission.[96] Polycarbonate, poly(methyl methacrylate), and epoxy show degradation under UV and visible light through different pathways. Silicone degradation, like discoloration and embrittlement, is observed under UV light and is related to UV-induced generation of radicals.[108]

However, the debate is still open about the direct damage caused by photons during continuous LED operation. De Santi et al. investigated this topic on InGaN–GaN multiple quantum wells (MQWs) $1 \times 1 \, mm^2$ photodetectors, with 30 QWs.[109] These devices, that have a LED-like structure, can be used in wireless power transfer systems and must be able to

withstand optical intensities up to hundreds of W/cm². The authors stressed the devices under open-circuit conditions at 361 W cm⁻² for 486 h with a 405 nm continuous wave laser diode. During that time they evaluated the damage induced by the sole optical field because no current flowed across the device.

Figure 19 shows the photoluminescence of the sample before and after the stress. It is possible to see that there is a lowering in emission in the region of the device corresponding to the rectangular laser spot. Different degradation mechanisms were hypothesized, like surface reflectivity variation, thermal degradation, increase in carrier escape from QWs, or increase in defects. The first mechanism was excluded by observing that surface reflectivity had no variation due to the laser spot. The second mechanism was excluded by performing a purely thermal stress, resulting in a different degradation mechanism. As no current flowed across the device, the increase in escape was not a viable option to explain the degradation; therefore, the cause of the degradation was attributed to the purely optical-induced creation of defects in the active zone of the device. In particular, direct damage of gallium nitride lattice was excluded because the damage was caused by 3.06 eV photons (405 nm) and GaN bond energy is around 8.9 eV.[110] One possible process that leads to optically induced degradation is the breaking of V_{Ga}–H_n complexes, creating deep acceptor levels that increase SRH recombination.

From **Figure 20** it is possible to note that optical stress increased photoluminescence in the yellow region (550-600 nm), whereas pure thermal stress does not affect luminescence in this region. This supports the hypothesis that optical stress increases optical active gallium vacancies[37] or their complexes with carbon or oxygen.[111,112]

4.3. Diffusion-Related Degradation

4.3.1. Visible GaN Emitters

As discussed above, a decrement in the optical performance of LEDs can be ascribed to the generation of defects that lead to an increment in the nonradiative SRH recombination rate. One possible explanation for the formation of these defects is the diffusion of impurities into the active region, moving from the p-side toward the n-side of the structure.[113] In particular, typical diffusing impurities are magnesium and/or hydrogen. Mg is commonly used as p-dopant in GaN. Due to its high
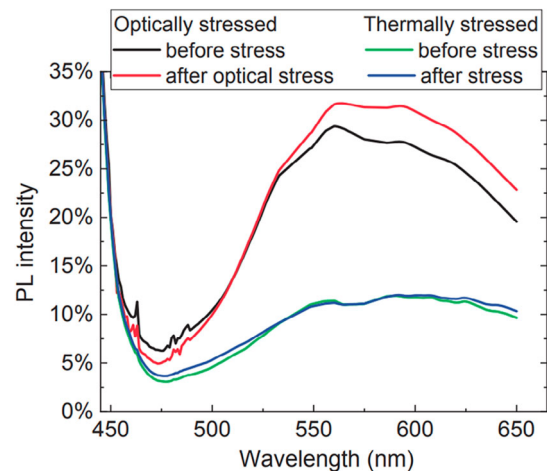
Figure 20. Photoluminescence spectral distribution of unstressed device under purely optical (black line unstressed, red line stressed) and purely thermal (green line unstressed, blue line stressed). Reproduced with permission.[109] Copyright 2018, The Japan Society of Applied Physics.

activation energy, ranging between 120 and 160 meV,[114–117] the GaN epilayer needs to be heavily doped with Mg to obtain a sufficient density of holes. High concentrations of Mg can favor its diffusion and Mg-related optical losses.[66,114] Additionally, Mg atoms tend to bond with H atoms present in the growth chamber. Depending on their nature,[118] the metastable Mg—H and Mg–lattice bonds can be broken by temperature and carrier energy: in this case there is an increment in the effective doping level and some H atoms are free to move inside the lattice. Mg—H complexes and hydrogen atoms (H^+ and H^0) are more commonly found in interstitial position. Diffusion of substitutional atoms is less likely than diffusion of interstitial because in the former condition more energy is required to break the chemical bonds and move the atom to an interstitial position, where it can more easily propagate.[119] The role of a diffusive process in device degradation has been often related to the dependence of the optical power decay on the square root of stress time.[65,119,120] In fact, diffusion in one dimension is explained by Fick's second law. The model to explain the relation between the local concentration of the diffusing species N_{diff}, position, and time, assuming that the concentration at the
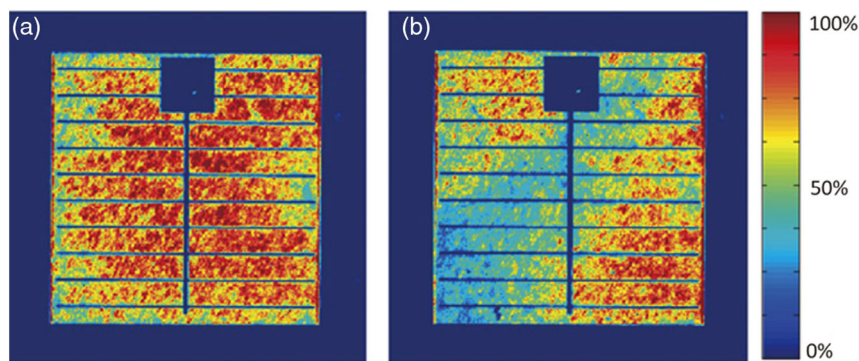
Figure 19. a) Photoluminescence of unstressed device and b) 486 h stressed device. Reproduced with permission.[109] Copyright 2018, The Japan Society of Applied Physics.

starting point is constant and equal to N_0, is expressed by the following formula

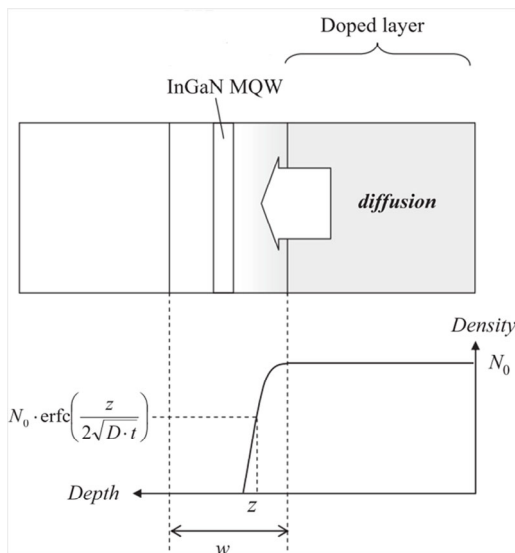$$N_{\text{diff}} = N_0 \text{erfc}\left(\frac{z}{2\sqrt{Dt}}\right) \tag{14}$$

where z is the position, D is the diffusion coefficient, and t is the time.[119,121]

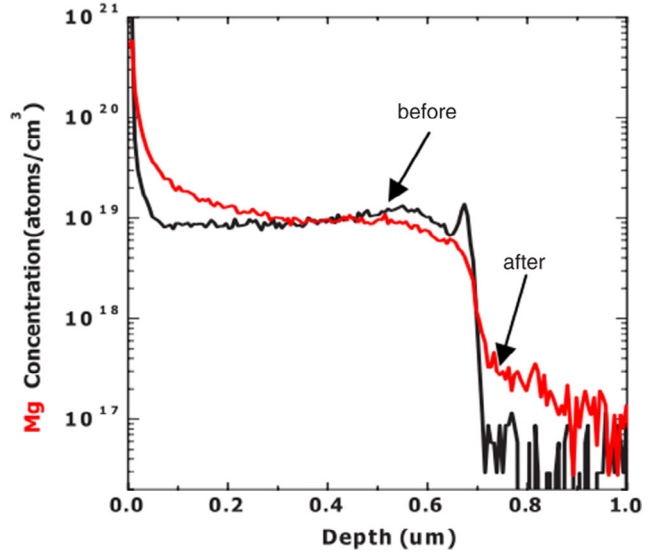**Figure 21** shows the diffusion mechanism and profile of defects within a SQW structure, based on Equation (14).

A similar trend has been observed in the degradation of AlGaInN laser diodes by Nam et al.[122] As shown in **Figure 22**, the authors have demonstrated through secondary ion mass spectrometry (SIMS) analysis that Mg dopant diffuses and accumulates into the active layer. This process favors the increment of point defects such as vacancies, Mg interstitials, or their complexes, thus inducing the increase in the rate of nonradiative SRH recombination. In the following years, Marona et al.[123] analyzed similar samples, finding that no apparent variation in the concentration of Mg was occurring during aging, and therefore leaving the discussion on Mg migration in III-nitrides still open.

Nam et al.[122] have also suggested the hypothesis that dislocations act as possible diffusion paths for Mg atoms. Lee et al.[66] have further investigated on this aspect by comparing the degradation rates of different LDs and LEDs grown on GaN and sapphire substrates. The latter group of devices, which exhibited a higher dislocation density due to the higher lattice mismatch between sapphire and the epitaxial GaN material, showed faster degradation. Through SIMS analysis, the authors could prove that during the aging process Mg atoms were diffusing more in samples featuring higher dislocation density, indicating that extended defects may act as pathways for the diffusion of Mg (**Figure 23**).
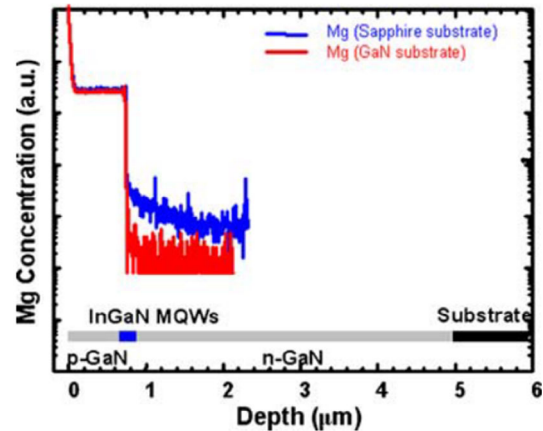
The observed increment in the concentration of Mg-related nonradiative recombination centers was assumed to be the cause

Figure 22. Mg SIMS profile of a GaN laser diode sample before and after degradation. Reproduced with permission.[122] Copyright 2004, Wiley-VCH.

Figure 23. Comparison of the SIMS depth profile of Mg in the devices grown on sapphire substrate and GaN substrates. Reproduced with permission.[66] Copyright 2008.

Figure 21. Model of the diffusion of impurities acting as NRRCs from one side of the junction toward the active region of a GaN laser diode. Reproduced with permission.[121] Copyright 2012, IEEE.

of the observed reduction in the EL intensity. Therefore, from these results, the authors suggested that the diffusion of Mg atoms through dislocations, and the subsequent generation of Mg-related NRRCs in the active layer, is one of the main gradual degradation mechanisms limiting the reliability of visible LEDs/LDs.

Also, Castiglia et al.[124] have analyzed the impact that high Mg doping level has on the electrical and optical degradation of superluminescent LEDs emitting at 405 nm. Devices featuring a highly ($[\text{Mg}] = 4 \times 10^{19}\,\text{cm}^{-3}$) p-doped structure show stronger degradation of the electrical characteristics during constant current stress at $J = 4\,\text{kA}\,\text{cm}^{-2}$ at room temperature, with respect to devices featuring a halved Mg concentration. SIMS analyses revealed that no diffusion of Mg occurred during stress, whereas a $\approx 10x$ decrease in H concentration could be observed.

The authors ascribed the strong increase in operating voltage of the devices during the first 100 h of stress to the diffusion of hydrogen toward the p-side, and to the subsequent passivation of Mg acceptor at the p-metal/semiconductor interface. The following partial recovery of the operating voltage was then ascribed to the slow hydrogen removal from the GaN layer through the p-metal. Their finding highlighted the possible role of H diffusion in the degradation of InGaN LEDs and LDs. Evidence of diffusion-related degradation was also reported by La Grassa et al.[113] During a constant-current stress test carried out on blue GaN LEDs, the authors observed a reduction in the emitted optical power that showed a square root dependence on time, which supported the hypothesis of a defect diffusion process. Capacitance–voltage measurements also revealed an increase in the junction charge due to an accumulation of free charge in the active region. As shown in **Figure 24**, this variation was found to be linearly correlated with the increase of the SRH coefficient, whose trend followed the square root of time stress.

These results supported the hypothesis that optical degradation is caused by the diffusion of charged defect/impurities toward the active region. These impurities, either Mg- or H-related, generate deep levels that behave as efficient nonradiative recombination centers. This hypothesis was further confirmed by DLTS measurement, which highlighted a reduction of shallow defects and the formation of deep traps with higher activation energy during stress.

4.3.2. Diffusion-Related Degradation in UV LEDs

Several articles report on the role of hydrogen and magnesium[54,57,125,126] as responsible of a series of degradation processes in GaN LEDs. Recently, the work of Glaab et al.[23] confirmed that H ions are much more prone to diffuse across the device structure during aging of UV LEDs. This is demonstrated by the SIMS profiles of a 310 nm UV-B LED measured during a constant current stress carried out at 100 mA for 100 h, as reported in **Figure 25**.

The authors identified a first decrease in H concentration at the p-side and in the active region after 10 h of stress test, which was ascribed to the migration of H toward the n-side. The generation of these free H ions was ascribed to the breaking of H-containing defect complexes (mostly in the EBL), possibly
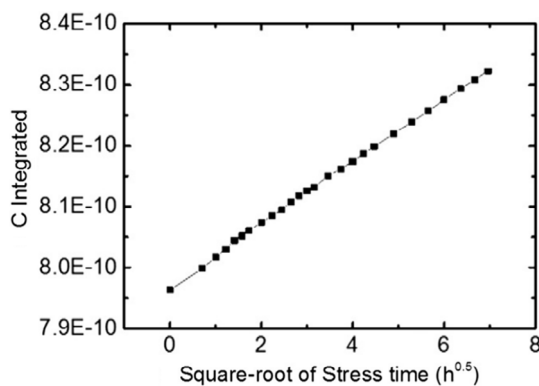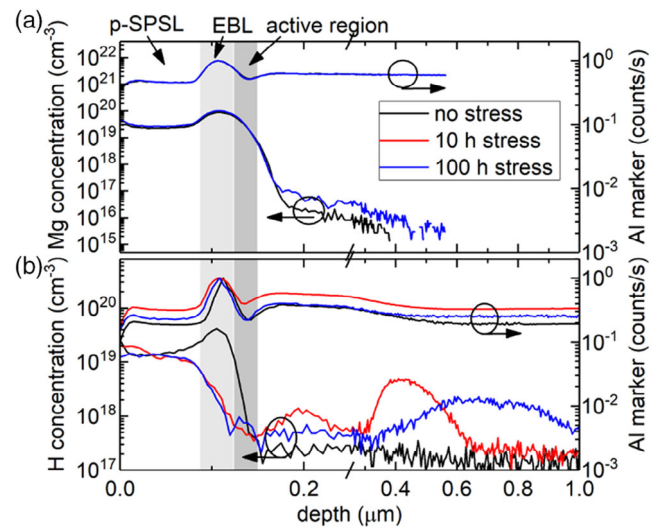
Figure 25. a) Mg and b) H concentration depth profiles at 0, 10, and 100 h of operation determined by SIMS on UV-B LEDs during a constant current stress at 100 mA. Reproduced with permission.[23] Copyright 2019, IEEE.

caused by the interaction with hot carriers. By repeating the measurement after 100 h of stress, the authors also found that the diffusion of hydrogen was still taking place: the process was found to be correlated to the changes in the optical power and drive voltage of the LEDs, and was tentatively ascribed to the generation of point defects in the active region. The authors did not find any relevant variation in the Mg profile during the test, so they concluded that the Mg ions did not diffuse in the structure after the growth of the device.

4.4. Lifetime Prediction

The gradual degradation of electronic and optoelectronic devices and components can be accelerated by several factors, including temperature, electric field (or voltage), current density, and humidity. From a reliability standpoint, the impact of such driving forces on the lifetime prediction of a given device is mathematically considered by extrapolating the so-called acceleration factor (AF).[127] This quantity represents the ratio between the degradation rates, or equivalently between the inverse mean time-to-failure (MTTF), in a given stress/usage scenario and a milder one. The cumulative effect of the aforementioned degradation forces can be accounted for by levering the Eyring model,[127] which is based on the Nernst–Einstein relation describing processes and reactions in specific materials. In its simplest form, this model postulates that the various stress forces acting on the devices are independent, and that their impact on the lifetime can be mathematically considered by multiplying the basic AF by functions of various types (i.e., exponential, power-law, Arrhenius-like, etc.) each depending on the specific stress force applied. An expression for the AF resulting from the cumulative effect of temperature and current density, typically employed for the analysis of the reliability of laser diodes and LEDs, is given by

Figure 24. Integrated junction charge in function of the square root of stress time. Reproduced with permission.[113] Copyright 2016, Elsevier.

$$AF = \left(\frac{J_{acc}}{J}\right)^n \cdot \exp\left[\frac{E_a}{k_b}\left(\frac{1}{T_j} - \frac{1}{T_{j\_acc}}\right)\right] \qquad (15)$$

where J, T_j, J_{acc}, and T_{j_acc} are the current densities and junction temperatureas under nominal and accelerated stress conditions.[127,128] The first power-law term accounts for current-density induced acceleration on the degradation rate, stronger for higher values of n, whereas the second exponential term expresses the canonical Arrhenius-like dependency of a physical process on temperature, with E_a representing the extrapolated thermal activation energy of the process. The range of variability of the n and E_a indexes strongly depends on the type and maturity of the devices under test, as well as on the adopted stress conditions. This dependency is evidenced by the spread of the n and E_a values reported in **Table 3**.

The specific functional dependencies expressed by Equation (15) are strictly related to the statistical model employed to analyze the lifetime data, and to the physical processes assumed to be driving device/component degradation. This type of reliability analysis offers the greatest accuracy in terms of lifetime estimation, but requires a tight control and estimation of the physical driving forces of the degradation within the devices during the accelerated life tests. As this kind on information is typically not available to the end user of the electronic devices, e.g., to manufacturers of solid-state luminaries or of lighting components, different standards have been developed in order to provide guidelines for the measurements and lifetime estimation of GaN LED-based lighting solutions. Within this field, the most widely adopted standards are represented by the IES LM-80-08 and TM-21-11, as well as their annexes and revisions (IES LM-84 and TM-28).[129–132] In summary, these standards define the lumen maintenance testing conditions in terms of sampling period (500–1000 h), minimum total sampling time (typically between 3000 and 6000 h), and the ambient aging temperature (indicatively from 25 to 85 °C); conservative stress conditions are typically suggested in order to avoid the turn-on of degradation processes which do not take place during nominal operation of the tested light source. In addition to that, guidelines for the L70 projection are typically defined on the basis of the sole thermal acceleration (Arrhenus-like AF), therefore may not be suitable in scenarios where the dominant degradation force is not temperature.

4.5. Catastrophic Degradation Induced by Electrical Overstress

Gradual degradation of the LED chip does not represent the only reliability concern for modern GaN-based visible LEDs. With the improvement of crystal quality, device efficiency, and thermal management capabilities of the LED packages, the lifetime limiting factors moved from the semiconductor chip itself to other extrinsic elements of the LED system, such as the reflector, the encapsulant, or the embedded phosphors.[91,133] In addition to that, sudden failures of the devices rather than their gradual worsening have become the major issue, as far as the useful operating lifetime in the field is concerned. This kind of failures typically arises from electrical overstress events, namely, EOSs.[25,134] Generally speaking, an EOS event represents a temporary bias condition during which the maximum electrical ratings of the LED are exceeded. During this time frame, which can last from tenths or hundreds of ns, as in the case of electrostatic discharges (ESDs),[135] to several ms,[25] the excess energy and/or power released in overstress condition can induce a sudden drop in the optical performance of the device, limit its long-term reliability,[136] and even induce its immediate failure.[137] In the first two cases, the failure is typically referred to as a "soft" failure process, whereas in the latter case the catastrophic event is called "hard" failure.[135] A specific family of EOS events is represented by ESDs. During these events the excess energy is released toward the device as a consequence of a fast, i.e., shorter than 100 ns, charge transfer process originating from the human body, a machine, or the environment. As far as GaN LEDs are concerned, it has been demonstrated that reverse-bias ESD events represent a stronger concern compared to forward-bias events, due to the fact that in the former condition the high electric field applied to the depleted junction of the device in a blocking state can favor its breakdown.[135,138] This process is typically favored in devices featuring higher crystalline defectiveness: as higher indium content in the well is typically associated with higher defects concentrations, due to the higher lattice mismatch and material strain (see Section 3.2), this ultimately determines a lower robustness of GaN LEDs emitting in the green region toward ESD events, as also testified by the data reported in **Figure 26**.

In order to improve their robustness against ESD events, mid- and high-power LEDs typically rely on external protection

Table 3. Values of temperature- and current-related acceleration coefficients for various types of GaN-based LEDs. The L50 and L70 failure criterion indicate that a status of failure of the device was assumed to be reached once the OP of the emitters decreases by 50% or 30%, respectively.

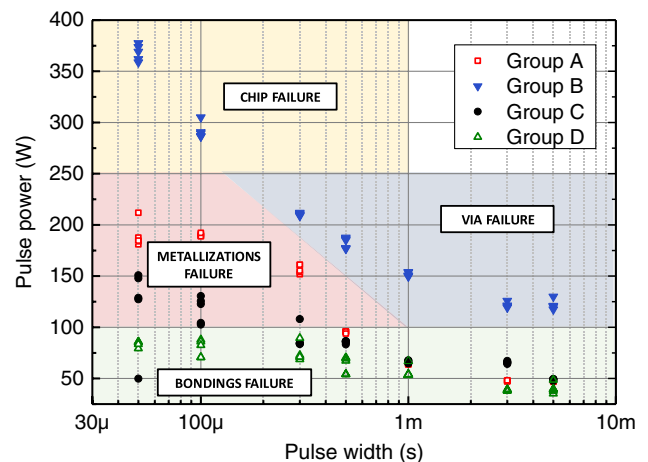| Sample	Criterion	Aging conditions	E_a [eV]	n	Year	Ref.
HB blue LEDs	L50	700–900 mA, $T = 25$ °C		4.1–5.5	2021	[153]
White midpower LEDs	L70	60 mA, $T = 55$–75 °C	0.51		2018	[154]
White LEDs, 1 mm^2	L70	350 mA max, variable RH (65–95%), $T = 120$ °C	0.5	0.44–0.7	2017	[128,155]
SSL lamps	L70	Variable RH	0.65-0.8		2016	[129]
LED strip lamps	L70	$T = 85$–107 °C	1.05		2016	[130]
475 nm LEDs, $I_{max} = 36$ mA	L50	20 mA, 70% RH, $T = 120$–140 °C	0.97		2016	[156]
	L50	10–30 mA, 70% RH, $T = 130$ °C		0.34		
HB LEDs	L70	$T = 160$–180 °C, 350 mA	0.35		2014	[157]
HB LEDs	L70	$T = 110$–170 °C	0.65		2014	[131]
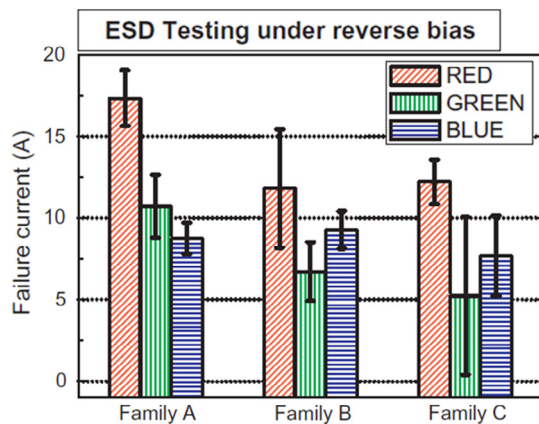
Figure 26. Comparison between average failure current of RGB LEDs submitted to reverse-bias ESD tests. Reproduced with permission.[135] Copyright 2013, Elsevier.


Figure 27. Dependency of failure pulse power on pulse width, for four different types of commercially available high-power LEDs. Reproduced with permission.[137] Copyright 2017, IEEE.

circuitry, such as a diode connected in antiparallel. As this approach is not beneficial in terms of cost and manufacturing complexity, several chip-level ESD mitigation strategies have been studied and adopted. These include, not being limited to, the tuning of the electron blocking layer thickness,[139] the insertion of a current blocking layer,[140,141] the modification of the epitaxial structure,[142,143] the improvement of the mesa isolation,[144] the reduction in concentration of V-shaped defects in the active region,[145] the optimization of the electrodes,[146] and the addition of floating guard rings.[147]

If the temporal duration of the unwanted bias state exceeds the microsecond scale, the condition is referred to as conventional EOS event. Buffolo et al.[137] have demonstrated that, for EOS pulses ranging from 50 μs to 5 ms, the onset of failure 1) strongly depends on the layout and structure of the device, and 2) is related to the robustness of extrinsic elements of the semiconductor chip, such as the vias, the metallizations, or the lateral passivation. For wider pulses, the excessive power dissipation was found to induce the melting of the bonding wires or the catastrophic failure of the vias, whereas shorter pulses evidenced the limited robustness of the semiconductor chip corners toward high electric fields (**Figure 27**). The authors ultimately found that high-power LEDs featuring a flip-chip structure without bonding wires offer the greatest robustness against the tested EOS range, evidencing how device-level optimizations can drastically help increasing the reliability of GaN LEDs in specific scenarios.

An electrical overstress condition can also occur when the device is operated above its maximum current rating for an extended period. This condition favors current crowding phenomena[148] that locally lower the radiative efficiency of the LED and accelerate device degradation. Recent studies have testified the localized degradation of the active region and/or of the current spreading layer occurring in this bias condition for various types of high-power LEDs by means of spatially resolved EL measurements.[87] **Figure 28** shows an example of such analysis: before stress, the EL measurement carried out at 1A shows that most of the optical emission occurs near the vias or the conducting edges of the chip. As the device is submitted to increasing levels of stress current, the emission, i.e., the

injected current, preferentially shifts toward the vias first, moving then toward the lower part of the semiconductor chip. As a consequence of device degradation, emission occurs far from both the edges and the vias, which are exactly the regions where current was preferentially flowing through in the unaged device. This variation in the spatial emission, along with the degradation of the series resistance, suggested that high temperature and current stress were inducing the localized worsening of the ohmic contacts, or of the current spreading layers of the device.

5. Conclusions

In conclusion, with this article we have reviewed the main lifetime-limiting mechanisms and issues affecting modern GaN-based LEDs. An extensive literature research, assisted by TCAD simulations, showed which are the worst types of defects in terms of SRH recombination, as well as the relative impact of their location within the active region of the device. We discussed that In-containing layers are a possible source of NRRCs and of other reliability issues in InGaN LEDs, and highlighted which are the possible mitigation strategies offered by current technology. As prolonged operation at high current levels favors both nonradiative recombination events and temperature-assisted processes, an overview of the degradation mechanisms assisted by high temperatures or driven by Auger recombination was provided. The analysis of the recombination-enhanced degradation mechanisms also included optically induced degradation, which was found to induce the formation of defects in the active region of GaN-based MQW devices. Finally, our review dealt with the analysis of the robustness of GaN LEDs under electrical overstress condition. In this case, we showed that LEDs based on mature technologies are prone to failure, due to the sudden degradation of extrinsic part of the GaN chip when EOS events occur in forward bias and for time periods longer than some tens of ms, whereas—for the samples under analysis—ESD-related failures impact the most under reverse-bias condition. In both
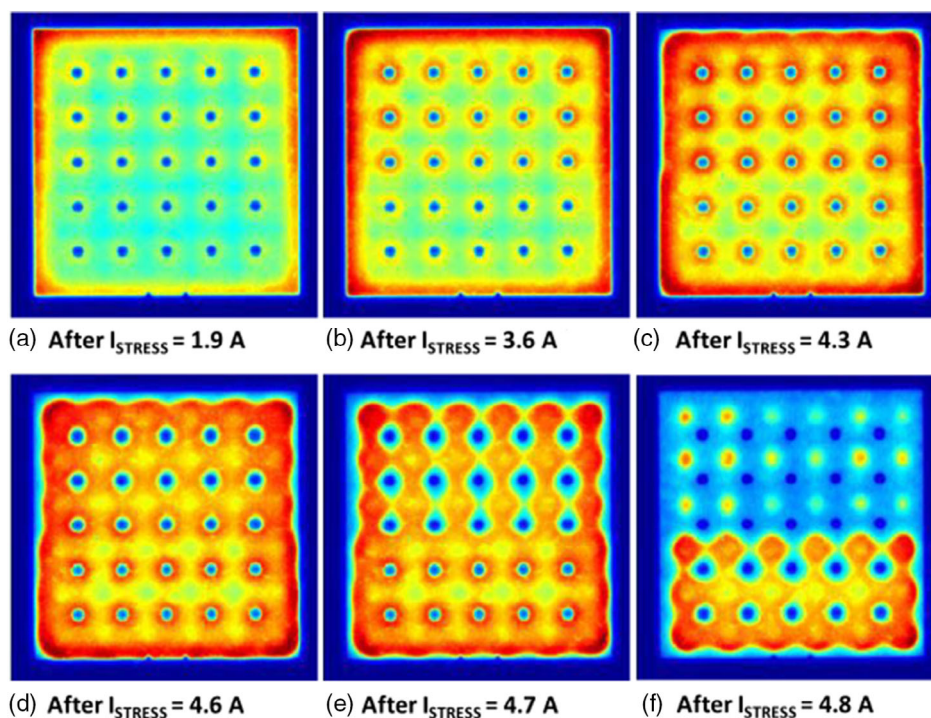
Figure 28. Normalized EL maps recorded at 1A after each step of the current step-stress experiment carried out on a high-power blue LED. Reproduced with permission.[87] Copyright 2020, IEEE.

cases, layout- and epitaxy-related optimizations can be employed to increase device robustness.

Conflict of Interest

The authors declare no conflict of interest.

[1] Y. Huang, E.-L. Hsiang, M.-Y. Deng, S.-T. Wu, *Light Sci. Appl.* **2020**, *9*, 1.
[2] P. J. Parbrook, B. Corbett, J. Han, T.-Y. Seong, H. Amano, *Laser Photonics Rev.* **2021**, *15*, 2000133.
[3] S.-L. Lee, C.-C. Cheng, C.-J. Liu, C.-N. Yeh, Y.-C. Lin, *J. Soc. Inf. Disp.* **2021**, *29*, 360.
[4] N. Trivellin, M. Buffolo, F. Onelia, A. Pizzolato, M. Barbato, V. T. Orlandi, C. Del Vecchio, F. Dughiero, E. Zanoni, G. Meneghesso, A. Crisanti, M. Meneghini, *Materials* **2021**, *14*, 2315.
[5] H. Inagaki, A. Saito, H. Sugiyama, T. Okabayashi, S. Fujimoto, *Emerg. microbes infect.* **2020**, *9*, 1744.
[6] M. Mori, A. Hamamoto, A. Takahashi, M. Nakano, N. Wakikawa, S. Tachibana, T. Ikehara, Y. Nakaya, M. Akutagawa, Y. Kinouchi, *Med. Biol. Eng. Comput.* **2007**, *45*, 1237.
[7] M. A. Würtele, T. Kolbe, M. Lipsz, A. Külberg, M. Weyers, M. Kneissl, M. Jekel, *Water Res.* **2011**, *45*, 1481.
[8] P. E. Hockberger, *Photochem. Photobiol.* **2002**, *76*, 561.
[9] A. Endruweit, M. S. Johnson, A. C. Long, *Polym. Compos.* **2006**, *27*, 119.
[10] J. W. Shi, K. L. Chi, J. M. Wun, J. E. Bowers, J. K. Sheu, *2016 IEEE Photonics Conf. IPC*, IEEE, Piscataway, NJ **2017**, p. 623, https://doi.org/10.1109/IPCON.2016.7831257.
[11] A. Pepe, C.-J. Chen, H. Y. Fu, K.-C. Chen, L. Wang, L. Wang, L. Zhang, M.-C. Wu, X. Liu, Y. Luo, Y. Dong, Z. Wei, L. Wang, Y. Luo, H. Y. Fu, H. Y. Fu, *Opt. Lett.* **2020**, *45*, 2616.
[12] L. Jinmin, L. Zhe, L. Zhiqiang, Y. Jianchang, W. Tongbo, Y. Xiaoyan, W. Junxi, *J. Semicond.* **2016**, *37*, 061001.
[13] J.-X. Guo, J. Ding, C.-L. Mo, C.-D. Zheng, S. Pan, F.-Y. Jiang, *Chin. Phys. B* **2020**, *29*, 047303.
[14] B. Tang, H. Xu, H. Wan, J. Miao, S. Zhou, Y. Liu, B. Tang, B. Tang, B. Tang, Y. Liu, H. Wan, H. Wan, J. Miao, J. Miao, *Opt. Express* **2019**, *27*, A1506.

[15] M. Cai, Z. Liang, Y. Qin, J. Fan, D. Ma, D. Yang, G. Zhang, *Opt. Mater.* **2020**, *107*, 110071.

[16] J. Huang, D. S. Golubović, S. Koh, D. Yang, X. Li, X. Fan, G. Q. Zhang, *IEEE Trans. Device Mater. Reliab.* **2015**, *15*, 220.

[17] A. M. Armstrong, M. H. Crawford, D. D. Koleske, *Appl. Phys. Express* **2014**, *7*, 032101.

[18] C. Haller, J. F. Carlin, G. Jacopin, D. Martin, R. Butté, N. Grandjean, *Appl. Phys. Lett.* **2017**, *111*, 262101.

[19] C. Haller, J. F. Carlin, G. Jacopin, W. Liu, D. Martin, R. Butté, N. Grandjean, *Appl. Phys. Lett.* **2018**, *113*, 111106.

[20] Z. L. Li, S. Tripathy, P. T. Lai, H. W. Choi, *J. Appl. Phys.* **2009**, *106*, 094507.

[21] N. Trivellin, F. Piva, D. Fiorimonte, M. Buffolo, C. De Santi, V. T. Orlandi, F. Dughiero, G. Meneghesso, E. Zanoni, M. Meneghini, *Electronics* **2021**, *10*, 1703.

[22] F. Piva, C. De Santi, M. Deki, M. Kushimoto, H. Amano, H. Tomozawa, N. Shibata, G. Meneghesso, E. Zanoni, M. Meneghini, *Microelectron. Reliab.* **2019**, *100–101*, 113418.

[23] J. Glaab, J. Ruschel, T. Kolbe, A. Knauer, J. Rass, H. K. Cho, N. Lobo Ploch, S. Kreutzmann, S. Einfeldt, M. Weyers, M. Kneissl, *IEEE Photonics Technol. Lett.* **2019**, *31*, 529.

[24] F. Piva, C. De Santi, M. Deki, M. Kushimoto, H. Amano, H. Tomozawa, N. Shibata, G. Meneghesso, E. Zanoni, M. Meneghini, *Photonics Res.* **2020**, *8*, 1786.

[25] R. Tuttle, in *LED Prof. 2014 Symp.*, Bregenz, Austria **2014**.

[26] A. Armstrong, T. A. Henry, D. D. Koleske, M. H. Crawford, K. R. Westlake, S. R. Lee, *Appl. Phys. Lett.* **2012**, *101*, 162102.

[27] A. David, N. G. Young, C. A. Hurni, M. D. Craven, *Phys. Rev. Appl.* **2019**, *11*, 031001.

[28] A. Armstrong, T. A. Henry, D. D. Koleske, M. H. Crawford, S. R. Lee, *Opt. Express* **2012**, *20*, A812.

[29] A. David, N. G. Young, C. Lund, M. D. Craven, *ECS J. Solid State Sci. Technol.* **2020**, *9*, 016021.

[30] A. Alkauskas, M. D. McCluskey, C. G. Van de Walle, *J. Appl. Phys.* **2016**, *119*, 181101.

[31] M. Lax, *J. Chem. Phys.* **2004**, *20*, 1752.

[32] R. Pässler, *J. Appl. Phys.* **2004**, *96*, 715.

[33] A. Chantre, G. Vincent, D. Bois, *Phys. Rev. B* **1981**, *23*, 5335.

[34] C. H. Henry, D. V. Lang, *Phys. Rev. B* **1977**, *15*, 989.

[35] D. V. Lang, *J. Appl. Phys.* **1974**, *45*, 3023.

[36] Z.-Q. Fang, G. C. Farlow, B. Claflin, D. C. Look, D. S. Green, *J. Appl. Phys.* **2009**, *105*, 123704.

[37] P. Kamyczek, E. Placzek-Popko, V. Kolkovsky, S. Grzanka, R. Czernecki, *J. Appl. Phys.* **2012**, *111*, 113105.

[38] L. Stuchlíková, J. Šebok, J. Rybár, M. Petrus, M. Nemec, L. Harmatha, J. Benkovská, J. Kováč, J. Škriniarová, T. Lalinský, R. Paskiewicz, M. Tlaczala, *Conf. Proc. - 8th Int. Conf. Adv. Semicond. Devices Microsystems, ASDAM 2010*, Smolenice, Slovakia **2010**, p. 135, https://doi.org/10.1109/ASDAM.2010.5666319.

[39] J. Barbolla, S. Dueñas, L. Bailón, *Solid. State. Electron.* **1992**, *35*, 285.

[40] J. Bollmann, A. Venter, J. Bollmann, A. Venter, *Phys. B* **2018**, *535*, 237.

[41] A. Y. Polyakov, N. B. Smirnov, A. V. Govorkov, E. A. Kozhukhova, A. M. Dabiran, P. P. Chow, A. M. Wowchak, I. H. Lee, J. W. Ju, S. J. Pearton, *J. Appl. Phys.* **2009**, *106*, https://doi.org/10.1063/1.3238508.

[42] O. Soltanovich, E. Yakimov, *Phys. Status Solidi Curr. Top. Solid State Phys.* **2013**, *10*, 338.

[43] E. M. Bourim, J. I. Han, *Electron. Mater. Lett.* **2015**, *11*, 982.

[44] N. D. Nguyen, M. Germain, M. Schmeits, B. Schineller, M. Heuken, *J. Appl. Phys.* **2001**, *90*, 985.

[45] P. Kozodoy, S. P. DenBaars, U. K. Mishra, *J. Appl. Phys.* **2000**, *87*, 770.

[46] M. Meneghini, L. Rigutti, L. R. Trevisanello, A. Cavallini, G. Meneghesso, E. Zanoni, *J. Appl. Phys.* **2008**, *103*, 063703.

[47] A. M. Armstrong, Investigation of Deep Level Defects in GaN_C and GaN_Mg in AlGaN_GaN Films, **2006**.

[48] S. D. Brotherton, *Solid State Electron.* **1976**, *19*, 341.

[49] F. Piva, C. De Santi, A. Caria, C. Haller, J. F. Carlin, M. Mosca, G. Meneghesso, E. Zanoni, N. Grandjean, M. Meneghini, *J. Phys. D. Appl. Phys.* **2020**, *54*, 025108.

[50] W. Shockley, W. T. Read, *Phys. Rev.* **1952**, *87*, 835.

[51] D. Bisi, M. Meneghini, C. De Santi, A. Chini, M. Dammann, P. Bruckner, M. Mikulla, G. Meneghesso, E. Zanoni, *IEEE Trans. Electron Devices* **2013**, *60*, 3166.

[52] P. Kessler, K. Lorenz, S. M. C. Miranda, J. G. Correia, K. Johnston, R. Vianden, *Hyperfine Interact.* **2010**, *197*, 187.

[53] A. Terentjevs, A. Catellani, G. Cicero, *Appl. Phys. Lett.* **2010**, *96*, 171901.

[54] S. F. Chichibu, A. Uedono, K. Kojima, H. Ikeda, K. Fujito, S. Takashima, M. Edo, K. Ueno, S. Ishibashi, *J. Appl. Phys.* **2018**, *123*, 161413.

[55] F. Manyakhin, A. Kovalev, A. E. Yunovich, *MRS Internet J. Nitride Semicond. Res.* **1998**, *3*, 53.

[56] D. C. Look, Z. Q. Fang, B. Claflin, *J. Cryst. Growth* **2005**, *281*, 143.

[57] C. E. Dreyer, A. Alkauskas, J. L. Lyons, J. S. Speck, C. G. Van De Walle, *Appl. Phys. Lett.* **2016**, *108*, 141101.

[58] H. Li, M. Huang, S. Chen, *J. Semicond.* **2020**, *41*, 032104.

[59] F. Piva, C. De Santi, M. Buffolo, M. Deki, M. Kushimoto, H. Amano, H. Tomozawa, N. Shibata, G. Meneghesso, E. Zanoni, M. Meneghini, *Proc. of the SPIE Photonics West 2021 Conf.* **2021**, *11686*, 85, https://doi.org/10.1117/12.2578134.

[60] M. Silvestri, M. J. Uren, M. Kuball, *Appl. Phys. Lett.* **2013**, *102*, 073501.

[61] A. R. Arehart, A. Corrion, C. Poblenz, J. S. Speck, U. K. Mishra, S. P. DenBaars, S. A. Ringel, *Phys. Status Solidi Curr. Top. Solid State Phys.* **2008**, *5*, 1750.

[62] A. Hierro, S. A. Ringel, M. Hansen, J. S. Speck, U. K. Mishra, S. P. DenBaars, *Appl. Phys. Lett.* **2000**, *77*, 1499.

[63] A. R. Arehart, T. Homan, M. H. Wong, C. Poblenz, J. S. Speck, S. A. Ringel, *Appl. Phys. Lett.* **2010**, *96*, 10.

[64] X. S. Nguyen, H. W. Hou, P. De Mierry, P. Vennéguès, F. Tendille, A. R. Arehart, S. A. Ringel, E. A. Fitzgerald, S. J. Chua, *Phys. Status Solidi Basic Res.* **2016**, *253*, 2225.

[65] M. Takeya, T. Mizuno, T. Sasaki, S. Ikeda, T. Fujimoto, Y. Ohfuji, K. Oikawa, Y. Yabuki, S. Uchida, M. Ikeda, *Phys. Status Solidi C Conf.* **2003**, *2295*, 2292.

[66] S. N. Lee, H. S. Paek, J. K. Son, H. Kim, K. K. Kim, K. H. Ha, O. H. Nam, Y. Park, *J. Electroceram.* **2009**, *23*, 406.

[67] W. A. Quitsch, D. Sager, M. Loewenich, T. Meyer, B. Hahn, G. Bacher, *J. Appl. Phys.* **2018**, *123*, 214502.

[68] T. Mukai, M. Yamada, S. Nakamura, *Jpn. J. Appl. Physics, Part 1 Regul. Pap. Short Notes Rev. Pap.* **1999**, *38*, 3976.

[69] F. A. Ponce, D. P. Bour, *Nature* **1997**, *386*, 351.

[70] H. Jia, L. Guo, W. Wang, H. Chen, *Adv. Mater.* **2009**, *21*, 4641.

[71] J. H. Ryou, P. D. Yoder, J. Liu, Z. Lochner, H. S. Kim, S. Choi, H. J. Kim, R. D. Dupuis, *IEEE J. Sel. Top. Quantum Electron.* **2009**, *15*, 1080.

[72] T. Langer, H. Jönen, A. Kruse, H. Bremers, U. Rossow, A. Hangleiter, *Appl. Phys. Lett.* **2013**, *103*, 022108.

[73] A. Uedono, S. Ishibashi, S. Keller, C. Moe, P. Cantu, T. M. Katona, D. S. Kamber, Y. Wu, E. Letts, S. A. Newman, S. Nakamura, J. S. Speck, U. K. Mishra, S. P. DenBaars, T. Onuma, S. F. Chichibu, *J. Appl. Phys.* **2009**, *105*, 054501.

[74] N. Roccato, F. Piva, C. De Santi, R. Brescancin, K. Mukherjee, M. Buffolo, C. Haller, J.-F. Carlin, N. Grandjean, M. Vallone, A. Tibaldi, F. Bertazzi, M. Goano, G. Verzellesi, G. Meneghesso, E. Zanoni, M. Meneghini, *J. Phys. D. Appl. Phys.* **2021**, *54*, 425105.

[75] A. M. Armstrong, B. N. Bryant, M. H. Crawford, D. D. Koleske, S. R. Lee, J. J. Wierer, *J. Appl. Phys.* **2015**, *117*, 134501.

[76] M. Meneghini, L. R. Trevisanello, G. Meneghesso, E. Zanoni, *IEEE Trans. Device Mater. Reliab.* **2008**, *8*, 323.

[77] W. Liu, C. Haller, Y. Chen, T. Weatherley, J.-F. Carlin, R. Butté, N. Grandjean, *Appl. Phys. Lett.* **2020**, *116*, 222106.

[78] S. C. Tsai, C. H. Lu, C. P. Liu, *Nano Energy* **2016**, *28*, 373.

[79] P. P. Michałowski, E. Grzanka, S. Grzanka, A. Lachowski, G. Staszczak, J. Plesiewicz, M. Leszczyński, A. Turos, *J. Anal. At. Spectrom.* **2019**, *34*, 1718.

[80] S. Y. Karpov, *Photonics Res.* **2017**, *5*, A7.

[81] T. Akasaka, H. Gotoh, T. Saito, T. Makimoto, *Appl. Phys. Lett.* **2004**, *85*, 3089.

[82] A. Y. Polyakov, C. Haller, R. Butté, N. B. Smirnov, L. A. Alexanyan, A. I. Kochkova, S. A. Shikoh, I. V. Shchemerov, A. V. Chernykh, P. B. Lagov, Y. S. Pavlov, J. F. Carlin, M. Mosca, N. Grandjean, S. J. Pearton, *J. Alloys Compd.* **2020**, *845*, 156269.

[83] C. Haller, J.-F. Carlin, M. Mosca, M. D. Rossell, R. Erni, N. Grandjean, *Appl. Phys. Express* **2019**, *12*, 034002.

[84] R. Butté, J.-F. Carlin, E. Feltin, M. Gonschorek, S. Nicolay, G. Christmann, D. Simeonov, A. Castiglia, J. Dorsaz, H. J. Buehlmann, S. Christopoulos, G. B. H. von Högersthal, A. J. D. Grundy, M. Mosca, C. Pinquier, M. A. Py, F. Demangeot, J. Frandon, P. G. Lagoudakis, J. J. Baumberg, N. Grandjean, *J. Phys. D. Appl. Phys.* **2007**, *40*, 6328.

[85] A. Y. Polyakov, C. Haller, N. B. Smirnov, A. S. Shiko, I. V. Shchemerov, S. V. Chernykh, L. A. Alexanyan, P. B. Lagov, Y. S. Pavlov, J.-F. Carlin, N. Grandjean, S. J. Pearton, *J. Appl. Phys.* **2019**, *126*, 125708.

[86] L. Liu, M. Ling, J. Yang, W. Xiong, W. Jia, G. Wang, *J. Appl. Phys.* **2012**, *111*, 093110.

[87] M. Buffolo, E. Davanzo, C. De Santi, N. Trivellin, G. Meneghesso, E. Zanoni, M. Meneghini, *IEEE Trans. Device Mater. Reliab.* **2020**, *20*, 429.

[88] H. H. Wu, K. H. Lin, S. T. Lin, *Microelectronics J.* **2012**, *43*, 280.

[89] K. Baran, A. Różowicz, H. Wachta, S. Różowicz, D. Mazur, *Energies* **2019**, *12*, 3941.

[90] R. Adhikari, D. Beyragh, M. Pahlevani, D. Wood, *Energies* **2020**, *13*, 4046.

[91] M. Buffolo, C. De Santi, M. Meneghini, D. Rigon, G. Meneghesso, E. Zanoni, *Microelectron. Reliab.* **2015**, *55*, 1754.

[92] N. Renso, C. De Santi, A. Caria, F. Dalla Torre, L. Zecchin, G. Meneghesso, E. Zanoni, M. Meneghini, *J. Appl. Phys.* **2020**, *127*, 185701.

[93] I. S. Romanov, I. A. Prudaev, V. N. Brudnyi, *Russ. Phys. J.* **2018**, *61*, 187.

[94] S. Limpijumnong, C. Van de Walle, *Phys. Rev. B* **2004**, *69*, 035207.

[95] M. Meneghini, L.-R. Trevisanello, U. Zehnder, G. Meneghesso, E. Zanoni, *IEEE Trans. Electron Devices* **2007**, *54*, 3245.

[96] M. Yazdan Mehr, A. Bahrami, W. D. van Driel, X. J. Fan, J. L. Davis, G. Q. Zhang, *Int. Mater. Rev.* **2020**, *65*, 102.

[97] M. Meneghini, M. Dal Lago, N. Trivellin, G. Meneghesso, E. Zanoni, *IEEE Trans. Device Mater. Reliab.* **2013**, *13*, 316.

[98] Z. Chen, Q. Zhang, K. Wang, X. Luo, S. Liu, *J. Semicond.* **2011**, *32*, 014007.

[99] J. Ruschel, J. Glaab, B. Beidoun, N. L. Ploch, J. Rass, T. Kolbe, A. Knauer, M. Weyers, S. Einfeldt, M. Kneissl, *Photon. Res.* **2019**, *7*, B36.

[100] A. C. Espenlaub, D. J. Myers, E. C. Young, S. Marcinkevičius, C. Weisbuch, J. S. Speck, *J. Appl. Phys.* **2019**, *126*, 184502.

[101] J. Piprek, *Phys. Status Solidi* **2010**, *207*, 2217.

[102] R. W. Lambert, T. Ayling, A. F. Hendry, J. M. Carson, D. A. Barrow, S. McHendry, C. J. Scott, A. McKee, W. Meredith, *J. Light. Technol.* **2006**, *24*, 956.

[103] OSRAM, n.d.

[104] P. G. Eliseev, H.-B. Sun, S. Juodkazis, T. Sugahara, S. Sakai, H. Misawa, *Jpn. J. Appl. Phys.* **1999**, *38*, L839.

[105] J.-H. Yoo, M. G. Menor, J. J. Adams, R. N. Raman, J. R. I. Lee, T. Y. Olson, N. Shen, J. Suh, S. G. Demos, J. Bude, S. Elhadj, *Opt. Express* **2016**, *24*, 17616.

[106] M. Ščiuka, M. Dmukauskas, T. Grinys, A. Melninkaitis, in *Optical Resistance of GaN and InGaN Thin Films* (Ed. G. J. Exarhos, V. E. Gruzdev, J. A. Menapace, D. Ristau, and M. J. Soileau), International Society for Optics and Photonics, Bellingham **2012**, p. 85300Y, https://doi.org/10.1117/12.977451.

[107] S. Elhadj, J. Yoo, R. A. Negres, M. G. Menor, J. J. Adams, N. Shen, D. A. Cross, I. L. Bass, J. D. Bude, *Opt. Mater. Express* **2017**, *7*, 202.

[108] H. R. Fischer, C. Semprimoschnig, C. Mooney, T. Rohr, E. R. H. Van Eck, M. H. W. Verkuijlen, *Polym. Degrad. Stab.* **2013**, *98*, 720.

[109] C. De Santi, A. Caria, N. Renso, E. Dogmus, M. Zegaoui, F. Medjdoub, G. Meneghesso, E. Zanoni, M. Meneghini, *Appl. Phys. Express* **2018**, *11*, 111002.

[110] S. Porowski, *Mater. Sci. Eng. B* **1997**, *44*, 407.

[111] A. Sedhain, J. Li, J. Y. Lin, H. X. Jiang, *Appl. Phys. Lett.* **2010**, *96*, 151902.

[112] J. L. Lyons, A. Janotti, C. G. Van de Walle, *Phys. Rev. B* **2014**, *89*, 035204.

[113] M. La Grassa, M. Meneghini, C. De Santi, E. Zanoni, G. Meneghesso, *Microelectron. Reliab.* **2016**, *64*, 614.

[114] Y. Nakano, T. Jimbo, *Phys. Status Solidi* **2002**, *0*, 438.

[115] N. M. Johnson, J. Walker, D. P. Bour, R. A. Street, W. Go, *Appl. Phys. Lett.* **1996**, *68*, 667.

[116] T. Tanaka, A. Watanabe, H. Amano, Y. Kobayashi, I. Akasaki, S. Yamazaki, M. Koike, *Appl. Phys. Lett.* **1994**, *65*, 593.

[117] S. N. Lee, J. Son, T. Sakong, W. Lee, H. Paek, E. Yoon, J. Kim, Y. H. Cho, O. Nam, Y. Park, *J. Cryst. Growth* **2004**, *272*, 455.

[118] A. Castiglia, J.-F. Carlin, N. Grandjean, *Appl. Phys. Lett.* **2011**, *98*, 213505.

[119] C. De Santi, M. Meneghini, G. Meneghesso, E. Zanoni, *Microelectron. Reliab.* **2016**, *64*, 623.

[120] M. La Grassa, M. Meneghini, C. De Santi, M. Mandurrino, M. Goano, F. Bertazzi, R. Zeisel, B. Galler, G. Meneghesso, E. Zanoni, *Microelectron. Reliab.* **2015**, *55*, 1775.

[121] K. Orita, M. Meneghini, H. Ohno, N. Trivellin, N. Ikedo, S. Takigawa, M. Yuri, T. Tanaka, E. Zanoni, G. Meneghesso, *IEEE J. Quantum Electron.* **2012**, *48*, 1169.

[122] O. H. Nam, K. H. Ha, J. S. Kwak, S. N. Lee, K. K. Choi, T. H. Chang, S. H. Chae, W. S. Lee, Y. J. Sung, H. S. Paek, J. H. Chae, T. Sakong, J. K. Son, H. Y. Ryu, Y. H. Kim, Y. Park, in *Phys. Status Solidi Appl. Res.*, John Wiley & Sons, Ltd, Hoboken, NJ **2004**, pp. 2717–2720.

[123] L. Marona, P. Perlin, R. Czernecki, M. Leszczyński, M. Boćkowski, R. Jakiela, T. Suski, S. P. Najda, *Appl. Phys. Lett.* **2011**, *98*, 1.

[124] A. Castiglia, M. Rossetti, N. Matuschek, R. Rezzonico, M. Duelk, C. Vélez, J.-F. Carlin, N. Grandjean, in *Gall. Nitride Mater. Devices XI*, SPIE, Bellingham **2016**, p. 97481V.

[125] C. G. Van de Walle, J. Neugebauer, *J. Appl. Phys.* **2004**, *95*, 3851, .

[126] A. Alkauskas, C. E. Dreyer, J. L. Lyons, C. G. Van de Walle, **2016**, https://doi.org/10.1103/PhysRevB.93.201304.

[127] M. Ohring, L. Kasprzak, *Reliability and Failure of Electronic Materials and Devices*, Elsevier **2014**, Hardcover ISBN: 9780120885749, eBook ISBN: 9780080575520.

[128] B. Yan, D. Teng, L. Liu, G. Wang, *18th Int. Conf. Electron. Packag. Technol. ICEPT*, Harbin, China **2017**, p. 759, https://doi.org/10.1109/ICEPT.2017.8046559.

[129] P. Lall, P. Sakalaukus, L. Davis, *Proc. - Electron. Components Technol. Conf.*, Las Vegas, USA 2016-August, p. 1342, https://doi.org/10.1109/ECTC.2016.273.

[130] A. Locke, J. Prendergast, D. Riordan, J. Walsh, D. Grattan, *2016 27th Irish Signals Syst. Conf. ISSC*, Londonderry, UK **2016**, https://doi.org/10.1109/ISSC.2016.7528445.

[131] Y. H. Yang, Y. F. Su, K. N. Chiang, *Thermomechanical Phenom. Electron. Syst. -Proc. Intersoc. Conf.*, Orlando, USA **2014**, p. 178, https://doi.org/10.1109/ITHERM.2014.6892278.

[132] Z. Zhike, C. Suming, C. Shasha, S. Tingting, L. Yuanhui, *2019 16th China Int. Forum Solid State Light. 2019 Int. Forum Wide Bandgap Semicond. China, SSLChina IFWS*, Shenzen, China **2019**, p. 225, https://doi.org/10.1109/SSLCHINAIFWS49075.2019.9019768.

[133] P. Appaiah, N. Narendran, I. U. Perera, Y. Zhu, Y. Wei Liu, *Opt. Mater.* **2014**, *46*, 6.

[134] K. T. Kaschani, *Microelectron. Reliab.* **2015**, *55*, 853.

[135] S. Vaccari, M. Meneghini, A. Griffoni, D. Barbisan, M. Barbato, S. Carraro, M. La Grassa, G. Meneghesso, E. Zanoni, *Microelectron. Reliab.* **2013**, *53*, 1510.

[136] T. Nan, P. He, L. Yin, J. Zhang, *2016 17th Int. Conf. Electron. Packag. Technol. ICEPT*, Wuhan, China **2016**, p. 1122, https://doi.org/10.1109/ICEPT.2016.7583322.

[137] M. Buffolo, M. Meneghini, A. Munaretto, C. De Santi, G. Meneghesso, E. Zanoni, *IEEE Trans. Device Mater. Reliab.* **2017**, *17*, 191.

[138] C. De Santi, M. Meneghini, M. Buffolo, G. Meneghesso, E. Zanoni, *IEEE Electron Device Lett.* **2016**, *37*, 611.

[139] C. H. Jang, J. K. Sheu, C. M. Tsai, S. C. Shei, W. C. Lai, S. J. Chang, *IEEE Photonics Technol. Lett.* **2008**, *20*, 1142.

[140] Y. Z. Chiou, T. H. Chiang, D. S. Kuo, S. J. Chang, T. K. Ko, S. J. Hon, *Semicond. Sci. Technol.* **2011**, *26*, 085005.

[141] K. H. Lee, Y. T. Moon, S. K. Oh, J. S. Kwak, *IEEE Photonics Technol. Lett.* **2015**, *27*, 149.

[142] K. Lee, C. R. Lee, T. H. Chung, J. Park, J. Y. Leem, K. U. Jeong, J. S. Kim, *J. Cryst. Growth* **2017**, *464*, 138.

[143] P. Li, H. Li, Y. Zhao, J. Kang, Z. Li, Z. Liu, X. Yi, J. Li, G. Wang, *IEEE Photonics Technol. Lett.* **2015**, *27*, 2004.

[144] M. Meneghini, A. Tazzoli, G. Mura, G. Meneghesso, E. Zanoni, *IEEE Trans. Electron Devices* **2010**, *57*, 108.

[145] T. H. Chiang, C. K. Wang, S. J. Chang, Y. Z. Chiou, T. K. Ko, T. K. Lin, S. P. Chang, *IEEE Photonics Technol. Lett.* **2012**, *24*, 800.

[146] S. L. Chen, *J. Disp. Technol.* **2014**, *10*, 779.

[147] S. Hwang, J. Shim, *Electron. Lett.* **2008**, *44*, 590.

[148] X. Quo, E. F. Schubert, *J. Appl. Phys.* **2001**, *90*, 4191.

[149] M. Meneghini, C. De Santi, A. Tibaldi, M. Vallone, F. Bertazzi, G. Meneghesso, E. Zanoni, M. Goano, *J. Appl. Phys.* **2020**, *127*, 211102.

[150] G. Martin, A. Botchkarev, A. Rockett, H. Morkoç, *Appl. Phys. Lett.* **1996**, *68*, 2541.

[151] P. G. Moses, C. G. Van de Walle, *Appl. Phys. Lett.* **2010**, *96*, 021908.

[152] M. Meneghini, M. Dal Lago, N. Trivellin, G. Mura, M. Vanzi, G. Meneghesso, E. Zanoni, *Microelectron. Reliab.* **2012**, *52*, 804.

[153] Z. Lu, W. Guo, M. Li, J. Deng, J. Tai, *2020 17th China Int. Forum Solid State Light. 2020 Int. Forum Wide Bandgap Semicond. China, SSLChina IFWS*, Shenzen, China **2020**, p. 232, https://doi.org/10.1109/SSLCHINAIFWS51786.2020.9308702.

[154] H. Cao, Z. Ma, B. Sun, X. Sun, C. Yang, X. Li, J. Wang, L. Zhao, *AIP Adv.* **2018**, *8*, 065108, .

[155] L. Liu, J. Yang, G. Wang, *14th Int. Conf. Electron. Mater. Packag. EMAP 2012*, Lantau Island **2012**, https://doi.org/10.1109/EMAP.2012.6507888.

[156] E. Nogueira, V. Orlando, J. Ochoa, A. Fernandez, M. Vazquez, *Microelectron. Reliab.* **2016**, *64*, 631.

[157] G. Lu, M. Hao, Y. Huang, H. Zhang, *Proc. Electron. Packag. Technol. Conf. EPTC*, Chengdu, China **2014**, p. 928, https://doi.org/10.1109/ICEPT.2014.6922799.

Matteo Buffolo received his master's degree in electronic engineering from the University of Padova in 2014, with a thesis on the analysis of the degradation mechanisms of GaN-based midpower white LEDs. In March 2018, he obtained his Ph.D. at the Department of Information Engineering, University of Padova, where he is actually working as a postdoc. His research interests focus on the reliability of lighting systems employing GaN-based devices (lasers and LEDs) and on the investigation of the degradation mechanisms that affect IR laser sources for integrated telecommunication applications.
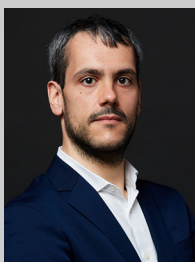
Alessandro Caria received his master's degree in physics from the University of Padova in September 2017 and his Ph.D. in information and communication science and technology from the University of Padova in February 2021, with a thesis on the physical phenomena limiting efficiency and reliability of InGaN–GaN multiple quantum well photodetectors and LEDs. He is currently a postdoc researcher at University of Padova, working on physics and reliability of III-nitride-based photodetectors and optoelectronic devices.

Francesco Piva is a Ph.D. student of the ACME group at the Department of Information Engineering, University of Padua. His main research filed is the ultraviolet light-emitting diodes (UV LEDs), where he studies their reliability, focusing on the defect generation during lifetime.

Nicola Roccato received his bachelor's degree in information engineering and in 2020 he obtained his master's degree in electronic engineering, both from the University of Padua. His master thesis focused on the analysis and TCAD simulations of the degradation behavior of InGaN–GaN LED. Currently, he is a Ph.D. student at the Department of Information Engineering, University of Padua, where he carries out research into the reliability and new characterization techniques of InGaN and near-UV LEDs.

Claudia Casu is a Ph.D. student in information engineering at the University of Padova, working on characterization, modeling, and reliability of GaN-based visible light-emitting diode. She received her master's degree in February 2020 at the University of Cagliari, with a thesis on "In-situ control of AlGaAs based DBR grown by MOVPE" at the Ferdinand Braun Institut in Berlin.

Carlo De Santi, since September 2019, holds an assistant professor position at the University of Padova. His main research activities focus on the characterization, modeling of physical processes, and reliability of electronic and optoelectronic devices based on elemental and compound semiconductors, including various ternary and quaternary compounds. The application fields of interest are power electronics and radio frequency systems, LEDs and lasers in the UV, visible monochromatic and white spectral range, devices for silicon photonics, solar cells and photodetectors, phosphors and systems for lighting applications. He is coauthor of more than 250 journal and conference papers, including 43 invited ones.

Nicola Trivellin received his B.S. and M.S. degrees in electronic engineering from the University of Padova, Padua, in 2007, and Ph.D. degree from the University of Padova in 2010. From 2011 to 2019, he was a postdoctoral research fellow at the Department of Information Engineering (DEI), University of Padova. He is currently an assistant professor at the Department of Industrial Engineering (DII), University of Padova. He has coauthored over 80 contributions and 10 inventions. His research interests include characterization and reliability study of optoelectronic devices, development of optoelectronic-based measurement systems, and innovative lighting based on optoelectronics for general lighting, biomedical, industrial, and space studies.

Gaudenzio Meneghesso graduated in electronics engineering at the University of Padova in 1992, working on the failure mechanism induced by hot electrons in MESFETs and HEMTs. Since 2011 he is with the University of Padova as full professor. His research interests involve mainly the electrical characterization, modeling, and reliability of microelectronics devices. Within these activities, he published more than 800 technical papers (of which more than 100 invited papers and 12 best paper awards).

Enrico Zanoni received the Laurea (cum laude) degree in physics from the University of Modena and Reggio Emilia, Modena, Italy, in 1982. He has been a full professor of digital electronics at the Department of Information Engineering, University of Padua, Padua, Italy, since 1997.

Matteo Meneghini received his Ph.D. in electronic and telecommunication engineering (University of Padova), working on the optimization of GaN-based LED and laser structures. Currently, he is an associate professor at the Department of Information Engineering, University of Padova. His main interest is the characterization, reliability and modeling of compound semiconductor devices (LEDs, laser diodes, HEMTs), and optoelectronic components, including solar cells. Within these activities, he has published more than 400 journal and conference proceedings papers.